DEVELOPMENT OF AN APPARATUS FOR ULTRAFAST THz SPECTROSCOPY

DEVELOPMENT OF AN APPARATUS FOR ULTRAFAST THz SPECTROSCOPY WITH INITIAL DEMONSTRATIONS OF SELECTED APPLICATIONS

By

CLARE L. ARMSTRONG, B.Sc.

A Thesis
Submitted to the School of Graduate Studies
in Partial Fulfillment of the Requirements
for the Degree
Master of Science

McMaster University

MASTER OF SCIENCE (2009) McMaster University
(Physics) Hamilton, Ontario

TITLE: Development of an Apparatus for Ultrafast THz Spectroscopy with Initial Demonstrations of Selected Applications

AUTHOR: Clare L. Armstrong, B.Sc.(University of Guelph)

SUPERVISOR: Dr. Harold K. Haugen

NUMBER OF PAGES: x, 85

Abstract

This thesis details the development of a multi-functional THz system capable of operating in three different geometrical configurations: transmission, reflection and attenuated total reflection (ATR). This apparatus can be used to collect THz time-domain spectroscopic data or it can be used to study the carrier dynamics of a system following optical excitation. These two functions categorize the two types of experiments presented in this thesis.

THz time-domain spectroscopy (TDS) was performed with the transmission and reflection configurations to determine the feasibility of using THz radiation to study thin polymer films. This technique was also performed in an ATR configuration with the use of a high purity Si prism. The THz ATR method was developed to extend the capabilities of the system to accommodate liquid samples. Water was the primary sample of interest, however methanol, ethanol and sucrose solutions were also examined. Although the results obtained regarding water are inconsistent with the literature, it has led to valuable insight as to how the current experimental setup may be improved.

The optical-pump, THz-probe technique was also incorporated with each of the configurations of the system. In transmission mode, the carrier dynamics of ZnSe nanowires were studied. In reflection mode, the optical-pump, THz-probe capabilities were tested using a Si wafer sample. In the ATR configuration, the carrier dynamics of the Si prism itself were examined. It is necessary to characterize the response of the prism to optical excitation if this technique is to be applied to samples placed on the surface of the prism. Efforts were made to control the free carrier lifetime of the near surface region of the Si prism, by irradiating the surface of the prism with a high energy proton beam to create defects in the Si. The results from this initial experiment, along with suggestions for future follow-up experiments, are presented.

Acknowledgements

I would like to thank my supervisor, Dr. Harold Haugen, for his support, guidance and for giving me the opportunity to work in an environment where I was able to develop as a researcher. I would also like to thank my committee members, Dr. John Preston and Dr. Kari Dalnoki-Veress, both of which, in addition to being on my committee, provided me with valuable insight and encouragement throughout the course of my degree.

There are a number of people who were directly involved with my research for whose input I am very grateful. I would like to thank Dr. Henry Tiedje for training me on the laser systems, helping with the design and construction of the THz system, and for being an invaluable resource. Thanks to Dr. Andrew Knights for performing the proton irradiation and lending his expertise on silicon. My lab mates, Eugene Hsu and Derek Sahota, were essential to my research experience. Eugene has been involved with virtually every step of this project and his expertise in the lab, along with his seemingly infinite patience, has been greatly appreciated. So much of this project would have been hindered without Derek's tremendous knowledge of THz data collection and analysis, and his willingness to sacrifice his time to engage in meaningful explanatory discussions. I would also like to thank my office mate, Nicholas Mailman, simply for being Nicholas Mailman.

There are many other people who have helped me throughout my M.Sc. that I would like to acknowledge. Thanks to Phil Ashby and Josh McGraw for always seeming to know when it was really important for me to leave my office and grab a coffee. Thanks to Allan Bayntun and Sandy Hsu for always making me welcome in their home when Manitoulin Island seemed too far away, and to James LeBlanc for helping me maintain my sanity.

I, of course, would like to extend my appreciation to my parents, Blaine and Maureen Armstrong, and my pseudo-mom, Veronika Bingaman, for giving me love and support, whether they could decipher what I was talking about or not. And last, but not least, I would like to thank Mr. Rob Cassibo: my teacher, mentor and friend. Not only has Cassibo been a constant source of inspiration, but he was the first to introduce me to this mess called physics.

Dedicated to
James Murray,
(1942-2009),
a man who truly appreciated
the pursuit of knowledge.

Contents

List of Figures

Chapter 1

Introduction

THz radiation is typically defined as the frequency range from 300 GHz to 30 THz, although most experimental work is performed in the 0.5 - 3 THz regime. THz radiation is submillimeter (10 μm to 1 mm) in wavelength and it has a photon energy range from $\sim$1.24 to 124 meV. As its location in the electromagnetic spectrum lies between microwave and infrared radiation (see Fig. 1.1), THz radiation bridges the gap between optical and electronic frequencies, thus posing difficulties in its generation and detection. While there are currently multiple techniques available to produce THz radiation [1], it is still a relatively unexplored region of the spectrum and the applications of THz radiation are still being realized.

THz radiation is beginning to carve out a niche for itself in a few areas such as imaging and spectroscopy. The fact that THz radiation is non-ionizing has made it particularly attractive in the medical imaging field. Its applications are somewhat limited by the fact that THz radiation is strongly absorbed by water, but it does still show potential in certain areas. For instance, this sensitivity to water gives rise to the possibility of differentiating between healthy and cancerous tissues. Tumorous tissues tend to have higher water content than healthy tissue, thus making them stronger absorbers of THz radiation and visible in a THz absorption image [2]. Dental imaging is also proving to be a promising candidate for the use of THz radiation. The enamel in teeth exhibit changes in refractive index as a result of mineral loss, and differences in the refractive indices of the enamel, dentine and pulp are detectable with THz radiation [3]. THz radiation is also proving to be useful for security imaging as most

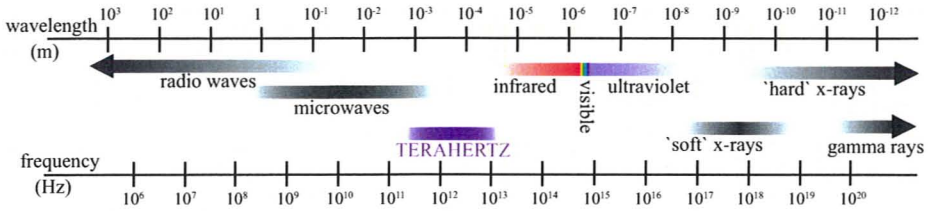

Figure 1.1: Schematic of the electromagnetic spectrum. THz radiation falls between microwave and infrared radiation, bridging the gap between the electrical and optical regimes of the spectrum.

plastics and clothing are invisible to THz radiation, while metal is highly reflective, making metallic weapons easily identifiable.

THz time domain spectroscopy has a wide range of applications [4]. Many molecular and crystal vibrational modes fall within the easily accessible THz regime, therefore, there is the potential to characterize the composition of a substance by its THz spectral fingerprint [5]. The generation and detection of ultrafast THz pulses have opened up the possibility of performing time resolved far-IR experiments. Unlike traditional spectroscopy, which simply measures intensity of the light that has interacted with a sample, THz spectroscopy measures the transient electric field. From the electric field, the amplitude and phase of the spectral components of the pulse can be extracted. This information can directly lead to the calculation of the complex refractive index, absorption coefficient and, subsequently, the complex dielectric function without the use of Kramers-Kronig analysis [6].

Another important application of THz radiation stems from the fact that photons in the THz regime have energies on the order of meV. This is a common energy scale for many electronic processes, making THz radiation an ideal probe. THz radiation has been used to examine changes in the optical conductivity of materials as they transition from the normal to the superconducting state [7, 8]. It can also be used to study carrier dynamics in semiconductors by optically exciting the sample while the THz pulse acts a probe to monitor the relaxation of the free carriers [9]. These two techniques have been combined to examine the destruction of a superconducting state via optical excitation as the THz pulse monitors the recovery of this state in superconducting thin films [10, 11].

1.1 Thesis Overview

This thesis presents work regarding the construction of an ultrafast THz radiation setup, as well as preliminary data obtained from this system. A versatile THz radiation generation and detection setup has been developed to accommodate a number of different experimental techniques. It is capable of functioning in a standard transmission mode as well as reflection and attenuated total reflection geometries with only minor modifications. These experimental geometries can also be coupled with optical-pump, THz-probe techniques. Because this project encompasses the development of a new apparatus, many of the experiments presented in this thesis are exploratory in nature. This was primarily an effort to test the capabilities of the system and to determine what techniques show promise for future experimental work.

Chapter 2 provides an introduction to the theoretical background relating to the generation and detection of THz pulses, attenuated total reflection (ATR), as well as the analysis of time domain spectroscopic data. Chapter 3 presents the experimental setup. A brief summary of the femtosecond laser system, which is required for the generation of THz radiation, is discussed. An overview of the newly constructed THz system is provided, including the subtle modifications required to change the geometry of the system to any of the following operating modes: transmission, reflection, or ATR. Diagnostics and preliminary results from the transmission and reflection experimental setups are presented and discussed in Chapter 4. These experiments explore the possibilities of examining polymer films using THz radiation. Chapter 5 is dedicated to the results obtained from the ATR geometry, focusing primarily on liquids and solutions. Water was analyzed in detail, however the results obtained for the dielectric function and complex refractive index were not in agreement with the literature. Various concentrations of sucrose solution were also examined using THz radiation in the ATR configuration. These results are presented, demonstrating the sensitivity of the system to changes in concentration. Optical-pump, THz-probe efforts are discussed in Chapter 6 and data from each of the experimental geometries is presented: ZnSe nanowires observed in transmission mode, Si in reflection, and a high purity Si prism in ATR. In order to effectively couple the optical-pump, THz-probe technique to the ATR geometry, the high resistivity float zone Si prism, required to satisfy the total internal reflection condition, had to be characterized under optical

excitation conditions. Efforts were made to control the free carrier lifetime of the near surface region of the Si prism. This was done by irradiating the surface of the prism with a high energy proton beam to create defects in the Si. The early stages of this experiment are also documented in this chapter. Much of the work described in Chapters 3 through 6 was presented at the Canadian Association of Physicists 2009 Congress and will be summarized in a brief article to appear in the fall edition of Physics in Canada. Finally, possible future work is presented in Chapter 7, as well as conclusive remarks.

Chapter 2

Theoretical Background

2.1 Generation of THz Radiation

While there now exists several different methods of generating THz radiation [12], many of these rely on an ultrafast change in polarization induced by a femtosecond laser pulse. The two most prevalent methods of generating THz radiation rely on ultrashort near-visible pulse irradiation of photoconductive antennae or optical rectification in nonlinear media.

The oldest method of generating THz radiation is through irradiation of photoconductive antennae [13, 14]. In this technique a voltage biased semiconductor is irradiated with an ultrashort laser pulse with an energy above the bad gap. This irradiation excites carriers into the conduction band, which are then accelerated in the applied electric field. The acceleration of the free charge produces an ultra-short current pulse and the changing polarization generates an electromagnetic pulse [15, 16].

THz generation via optical rectification in non linear media is the primary method of generation for the experimental work presented in this thesis; and thus, a more in-depth discussion of this process is presented in the following section.

2.1.1 Optical Rectification

In conventional optics the dipole moment density, or polarization, is linearly proportional to the electric field strength and the linear susceptibility.

$$P(t) = \chi^{(1)}E(t) \tag{2.1}$$

However, this expression can be generalized as a power series in the electric field,

$$P(t) = \chi^{(1)}E(t) + \chi^{(2)}E(t)^{(2)} + \chi^{(3)}E(t)^{(3)} + ... \quad . \tag{2.2}$$

The generation of THz radiation in a nonlinear medium is a second order nonlinear optical process known as optical rectification. Optical rectification (OR), or difference-frequency generation, is the result of wave mixing when light is incident on a nonlinear material. For example, considering the mixing of two distinct frequencies (ω_1 and ω_2), the electric field can be written,

$$E(t) = E_1 e^{i\omega_1 t} + E_1^* e^{i\omega_1 t} + E_2 e^{i\omega_2 t} + E_2^* e^{i\omega_2 t}; \tag{2.3}$$

where E_1 and E_2 are the respective field amplitudes, and E_1^* and E_2^* are their respective complex conjugates. Looking at the second order polarization,

$$P^{(2)}(t) = \chi^{(2)}E(t)^2, \tag{2.4}$$

the squared electric field expands out to yield the following terms,

$$\begin{aligned} E(t)^2 = {} & E_1^2 e^{i2\omega_1 t} + E_1^{*2} e^{-i2\omega_1 t} && (2.5)\\ & + E_2^2 e^{i2\omega_2 t} + E_2^{*2} e^{-i2\omega_2 t} && (2.6)\\ & + 2E_1 E_2 e^{i(\omega_1+\omega_2)t} + 2E_1^* E_2^* e^{-i(\omega_1+\omega_2)t} && (2.7)\\ & + 2E_1 E_2^* e^{i(\omega_1-\omega_2)t} + 2E_1^* E_2 e^{-i(\omega_1-\omega_2)t} && (2.8)\\ & + 2|E_1|^2 + 2|E_2|^2. && (2.9) \end{aligned}$$

The first four terms, Eq. 2.5 and Eq. 2.6, correspond to second harmonic generation (SHG), while Eq. 2.7 is related to the sum-frequency generation. Eq. 2.8 is the

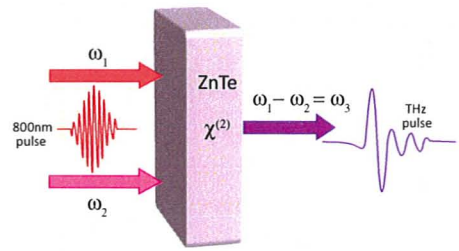

Figure 2.1: The broad bandwidth 800 nm pulse propagates through the ZnTe crystal where difference-frequency generation occurs creating THz radiation.

difference-frequency generation and the term of primary interest as it is responsible for the generation of THz radiation. Eq. 2.9 gives the DC rectification [17]. In this thesis, the nonlinear media used for THz radiation generation is a $\langle 1\ 1\ 0 \rangle$ oriented Zinc Telluride (ZnTe) crystal and it was irradiated with a broad bandwidth, 800 nm, femtosecond pulse. The mixing of the high frequencies with the low frequencies of the pulse yield difference-frequency generated radiation in the THz regime (see Fig. 2.1). It should be noted that while SHG and sum-frequency generation do occur, they generate frequencies that are above the band gap of ZnTe (2.25 eV or 552 nm) and are, thus, absorbed by the crystal upon generation.

Due to material dispersion, electromagnetic waves with different frequencies will experience different refractive indices. As a result of the birefringence of the material, an index ellipsoid can be used to describe the dependence of the relative magnitudes of the refractive indices, n^{ω_1} and n^{ω_2}, on the crystal orientation for each frequency component. Fig. 2.2 demonstrates that there exists a direction where the index ellipsoids of two different frequencies intersect. This leads to both frequencies of light experiencing the same refractive index and, therefore, having the same velocity when propagating through the crystal.

The orientation of the ZnTe generator crystal must be such that the incident 800 nm light and the generated THz radiation are phase matched to ensure efficient generation. When the 800 nm pulse and the generated THz pulse are phase mismatched, the destructive interference between the two pulses will drastically reduce the efficiency of the THz generation. The refractive index difference of the 800 nm pulse and the THz pulse can be minimized by rotating the crystal to maximize the coherence length of the conversion.

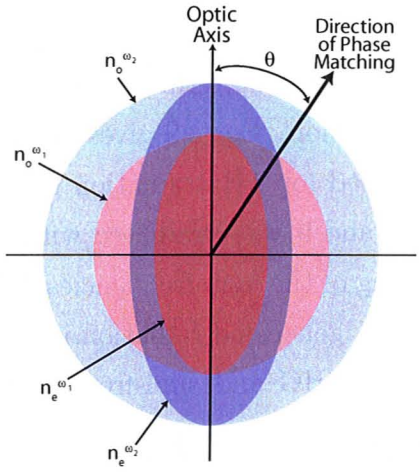

Figure 2.2: Birefringence is caused by crystallographic asymmetry resulting in a refractive index ellipsoid. The axes of the ellipsoid define the ordinary and extraordinary axes of crystal. These are sometimes referred to as the fast and slow optical axes, as the light propagating through the crystal will experience a different index of refraction, and subsequently travel at a different speed, depending on its initial polarization. The above figure demonstrates that there exists a direction where the $n_o^{\omega_1}$ and $n_e^{\omega_2}$ ellipsoids intersect, leading to both rays experiencing the same refractive index and, thus, having the same velocity when propagating through the crystal [18].

2.1.2 Air Plasma THz Radiation Generation

As an alternative to OR, THz radiation may also be generated from laser plasma [19]. A plasma can be created by focusing a high intensity laser pulse causing the ionization of air. Electrons are expelled from the region of high intensity electromagnetic field caused by the focused laser pulse via the ponderomotive force [20]. The acceleration of the ionized electrons result in an electromagnetic transient, thus producing radiation in the THz regime [21, 22]. With the current capabilities available in this lab, this method is not quite as effective as the more conventional methods of THz generation, as shown in Section 4.1, however it does have some promising advantages. Since the emitter target is the surrounding gas that is being ionized, it most likely exists in abundance. In addition to this, there is no worry of exceeding the damage threshold of the emitter target, as there is with the generator crystal in OR. This method of generation can be improved by applying a bias voltage across the air gap [23], or by implementing a nonlinear four wave rectification (FWR) technique, using both the fundamental and second harmonic frequencies to generate the plasma [24, 25, 26, 27]. More recently, the use of laser induced plasma has been extended to the detection of THz radiation [28]. With the use of shorter, more intense laser pulses, this method of generation can yield THz radiation with both high energy pulses and broadband width, comparable to other methods of generation using amplified table-top pulsed laser systems [29].

2.2 THz Radiation Detection - Electro-optic Sampling

The most common method of detecting THz radiation is through electro-optic sampling. This process is based on the Pockels effect, in which an electric field applied to a material induces birefringence. An 800 nm optical probe pulse passes though the detector crystal at the same time as some point in the THz pulse. The probe experiences a change in polarization due to the effect of the THz electric field on the detector crystal. This change in polarization of the probe pulse is linearly proportional to the amplitude of the THz electric field. As a result, by scanning the entire

Material	d(pm/V)	n_ν	n_{THz}	α_{THz} (cm^{-1})
GaP	24.8	3.18	3.34	1.9
ZnTe	68.5	2.87	3.17	1.3
$LiTaO_3$	161	2.145	6.42	46
$LiNbO_3$	168	2.159	5.16	16

Table 2.1: Electro-optic crystal properties. d is the non linear optical coefficient for optical rectification, n_ν is the refractive index at 800 nm, n_{THz} is the refractive index at 1 THz, and α_{THz} is the absorption coefficient at 1 THz [33]. From this data it is evident that ZnTe is a desirable candidate for electro-optic detection of THz radiation.

THz pulse through the optical probe, the THz temporal waveform can be mapped out [30].

Zinc-blende crystals, such as ZnTe and GaP, as well as $LiNbO_3$ and $LiTaO_3$ can be used for electro-optic detection (see Table 2.1). ZnTe is an effective detector crystal for this purpose [31] because it has a relatively high nonlinear optical coefficient for optical rectification, a refractive index in the far-infrared that is similar to its refractive index in the near-infrared, and a low absorption coefficient in the THz regime. These qualities minimize phase matching problems and yield a relatively efficient method of detecting THz radiation [32].

2.3 Attenuated Total Reflection

According to Snell's Law:

$$n_1 \sin\theta_i = n_2 \sin\theta_t; \tag{2.10}$$

where n_1 and n_2 are the refractive indices of the first and second medium, θ_i is the angle of incidence and θ_t is the angle of the beam transmitted in the second medium. Total internal reflection (TIR), as shown in Fig. 2.3, occurs when light strikes a boundary at an angle greater than the critical angle and the index of refraction of the second medium is less than the first ($n_{21} = n_2/n_1 < 1$),

$$\sin\theta_c = n_{21}. \tag{2.11}$$

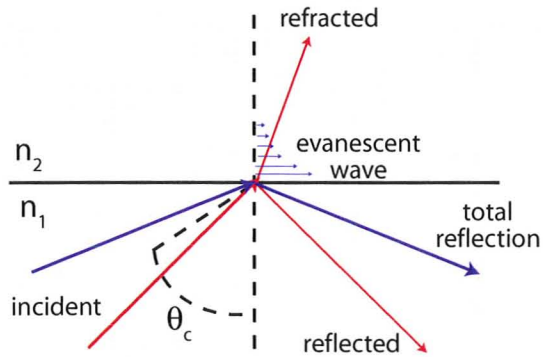

Figure 2.3: Schematic diagram of light striking a boundary between two media, where the index of refraction of the first, n_1, is greater than that of the second, n_2. The red ray shows the result of light incident on the boundary at an angle less than the critical angle, θ_c. In this scenario, some of the incident light is reflected, while the rest is refracted into the second medium. The blue ray demonstrates light incident on the boundary beyond the critical angle, resulting in total internal reflection. In this case, all of the light is reflected back into the first medium, however there is some penetration into the second medium by the resulting evanescent wave [34].

Because electromagnetic waves cannot be discontinuous at a boundary, an evanescent wave is produced, traveling along the boundary of the media when the TIR condition is achieved.

Consider light traveling in the xz-plane and incident on an interface in the xy-plane. The transmitted electric field,

$$E_t = E_o e^{i(\mathbf{k}_t \cdot \mathbf{r} - \omega t)}, \tag{2.12}$$

can now be written as follows,

$$E_t = E_o e^{i(k_t(x \sin\theta_t + z\cos\theta_t) - \omega t)}; \tag{2.13}$$

where $\mathbf{k}_t$ is the wave vector of the transmitted electric field. By applying Snell's Law (Eq. 2.10), $\cos\theta_t$ and $\sin\theta_t$ can be rewritten as

$$\cos\theta_t = i\sqrt{\frac{\sin^2\theta_i}{n_{21}^2} - 1} \qquad \text{and} \qquad \sin\theta_t = \frac{\sin\theta_i}{n_{21}}; \tag{2.14}$$

where it should be noted that $\cos\theta_t$ is purely imaginary when the angle of incidence is beyond the critical angle [35], satisfying the TIR condition (Eq. 2.11). Substituting Eq. 2.14 back into Eq. 2.13 yields an expression for the transmitted electric field when TIR occurs:

$$E_t = E_o e^{i\omega t} e^{ixk_t \sin\theta_i/n_{21}} e^{-z/d_p}; \quad \text{where} \quad \frac{1}{d_p} = k_t \sqrt{\frac{\sin^2\theta_i}{n_{21}^2} - 1}. \tag{2.15}$$

From Eq. 2.15, it can be seen that the evanescent wave is a standing wave that decays exponentially in the $\hat{z}$-direction. Even though the beam is totally reflected, there is some penetration into the second medium, although no net energy is transmitted through the boundary. The amplitude of the transmitted electric field decreases by a factor of 1/e when z=d_p, thus d_p is referred to as the penetration depth. The penetration depth is directly dependent on the wavelength of the incident light and diverges at the critical angle [36].

$$d_p = \frac{\lambda}{2\pi\sqrt{n_1^2 \sin^2\theta_i - n_2^2}} \tag{2.16}$$

Although the penetration depth does not depend on the polarization of the incident light, the strength of the interaction between the evanescent wave and the medium it penetrates into does depend on the polarization. It is, therefore, important to consider the effective thickness, which is the equivalent path length that would yield the same amount of absorption in a transmission experiment (see Fig 2.4).

$$d_{e\perp} = \frac{n_{21}\cos\theta\lambda}{\pi n_1(1-n_{21}^2)\sqrt{\sin^2\theta - n_{21}^2}} \tag{2.17}$$

$$d_{e\parallel} = \frac{n_{21}\cos\theta(2\sin^2\theta - n_{21}^2)\lambda}{\pi n_1(1-n_{21}^2)[(1-n_{21}^2)\sin^2\theta - n_{21}^2]\sqrt{\sin^2\theta - n_{21}^2}} \tag{2.18}$$

The evanescent waves from parallel and perpendicularly polarized incident electric fields of equivalent amplitude do not have the same amplitude in the penetrating medium [37]. The effective thickness of the parallel polarization is always greater and, therefore, should be used in experimental situations to maximize the interaction of the evanescent wave with the sample.

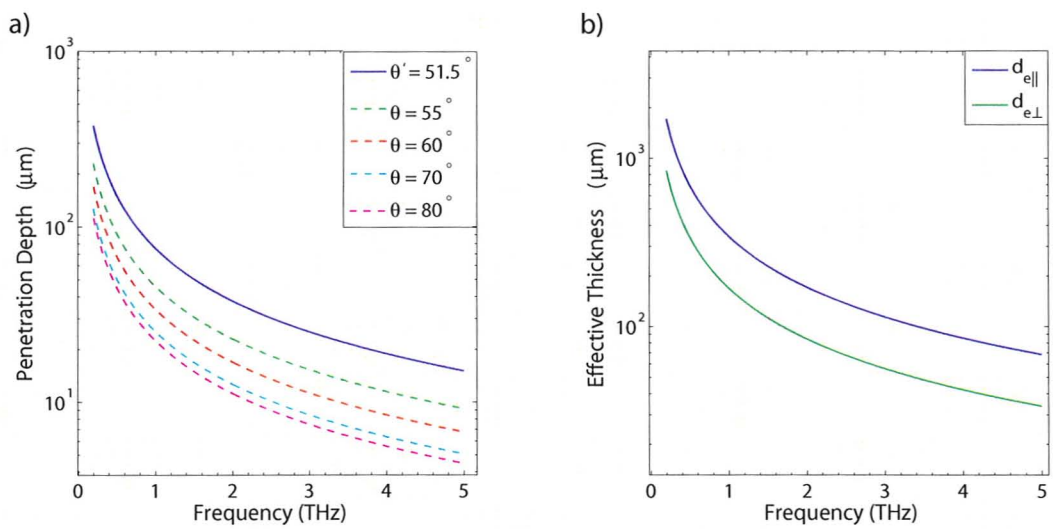

Figure 2.4: **a)** Penetration depth (Eq. 2.16) as a function of frequency for a refractive index ratio of n_{21}=0.702. This refractive index ratio is the same as a sample of index n_2=2.4 place on a Si ATR prism (n_1=3.42). Penetration depth increases as the critical angle (θ_c=44.6°) is approached. θ' is the incidence angle used with the Si prism in THz ATR experiments (see Chapter 5). **b)** Effective thickness as a function of frequency, displaying the difference between perpendicular (Eq. 2.17) and parallel (Eq. 2.18) polarizations of incident light at θ'.

2.4 Analysis

2.4.1 Time Domain Spectroscopy

Rather than probing a sample with one frequency at a time, time domain spectroscopy (TDS) interrogates the sample with a broad bandwidth THz pulse, which can be Fourier transformed to obtain the frequency spectrum. The spectral resolution obtained by the Fourier transform is dictated by the time length of the acquisition of the temporal waveform (i.e., short scans have a lower spectral resolution, therefore each bin in the Fourier transform will correspond to a larger range of frequencies). When taking the discrete Fourier transform of the temporal waveform the data must be windowed in some way. Applying a window to the data reduces discontinuity at the boundaries by ensuring that the endpoints of the data go smoothly to zero. The Fourier transform of a simple rectangular window results in a central peak with high side lobes that do not fall off very quickly, as shown in Fig. 2.5. Convolving the waveform with a rectangular window can cause spectral leakage as a result of these side lobes in the Fourier transformed window. To minimize the effects of spectral leakage, different windows can be chosen with less pronounced side lobes in their Fourier transform [38]. The analysis presented in this thesis convolves a Tukey window with the temporal data [39].

The size of the FFT window must be chosen carefully as to not truncate the THz waveform. Truncation can lead to spectral artifacts, such as a finite electric field amplitude at zero THz, implying that there is a DC offset. Fig. 2.6 displays the effects of a properly and improperly windowed temporal signal. In Fig. 2.6 b), the FFT of a properly windowed temporal waveform, has a zero frequency offset that is two orders of magnitude smaller than the spectral peak and within one order of magnitude of the noise floor. The FTT of the improperly windowed waveform, Fig. 2.6 d), shows an offset that is only one order of magnitude below the spectral peak and well above the noise floor, misleadingly implying that the signal at the near zero frequencies should be taken into consideration.

Although the THz spectral data appears to show a signal down to zero frequency, this is merely an effect of the FFT process and is not physical. The useful spectral data was considered to be the electric field amplitude that was at least 5× greater

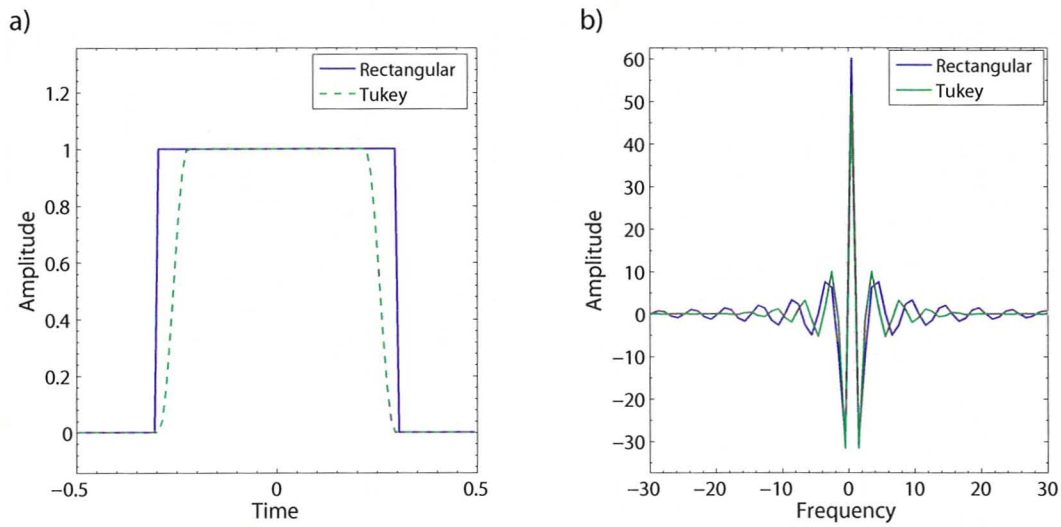

Figure 2.5: **a)** Rectangle and Tukey (tapered cosine) windows. **b)** Fourier transforms of these windows displaying the larger side lobes from the rectanglular window.

than the high frequency noise floor. For data collected under N_2 purge conditions, this typically resulted in a THz spectrum that ranged from ~0.2 - 2.8 THz (see Fig. 2.7). Almost all THz analysis is performed relative to a reference scan, which is why the pulse amplitudes are generally plotted in arbitrary units. By scanning in the absence of a sample, a convenient reference scan is created. This reference scan can then be compared to the sample scan allowing the extraction of information solely regarding the sample. This method, however, has both pros and cons. Taking data in this way minimizes the effects of systematic occurrences, which would generally present themselves in both the reference and the sample, and therefore would be divided out. Unfortunately, this is a time consuming process, as a reference scan may no longer be accurate if taken too far in advance of the sample. Problems such as laser drift and subtle changes in the environment, such as temperature and humidity, can create problematic differences between the reference and sample scans. To avoid this issue, one should try to take reference scans immediately preceding sample scans whenever possible.

Fig. 2.7 shows the effects of water vapour in both the temporal waveform and the frequency spectrum. In the temporal waveform the presence of water results in an attenuation in the amplitude of the main THz pulse. There is also substantial

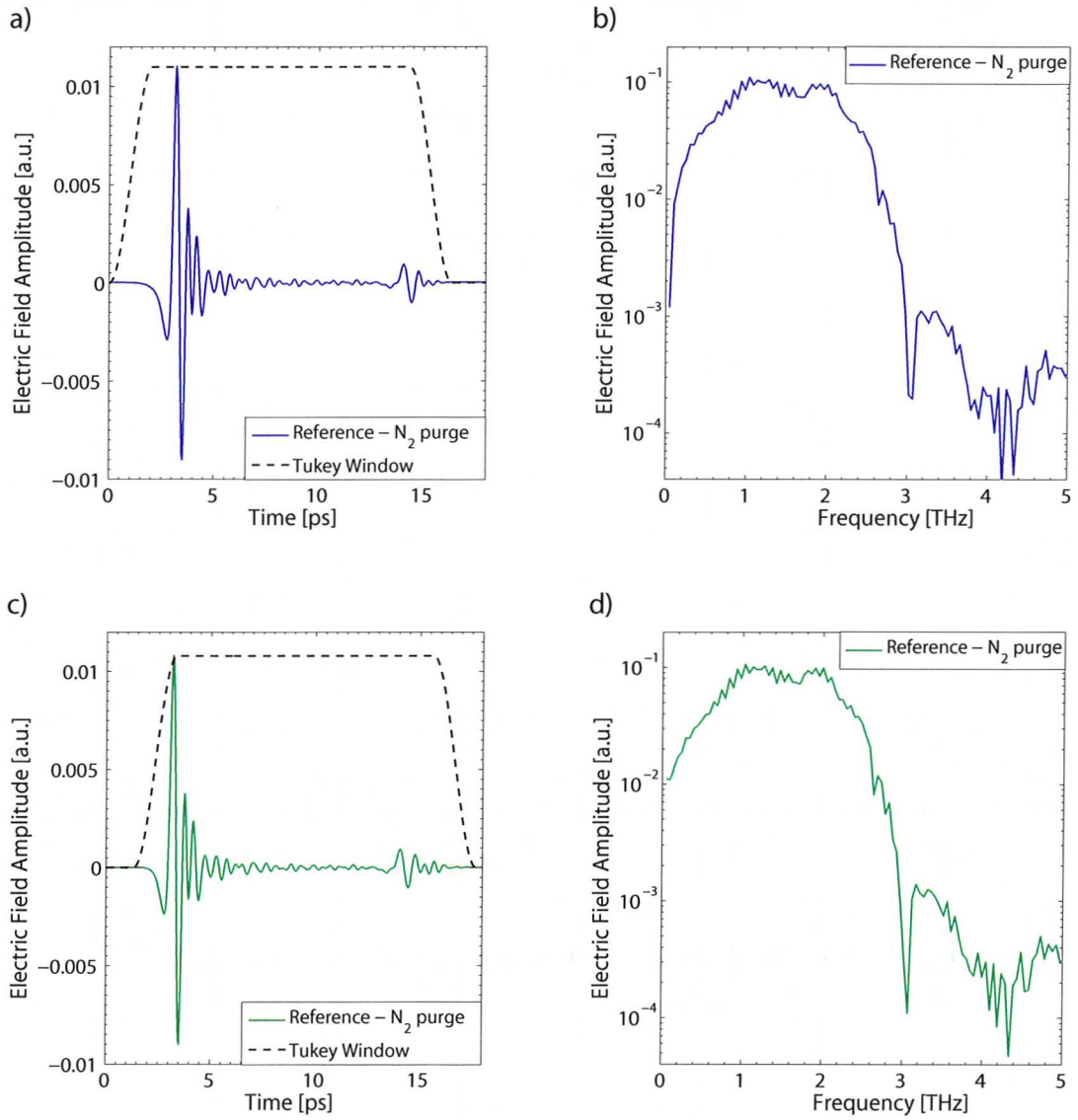

Figure 2.6: Transmission reference scan demonstrating the effect of truncating the temporal waveform when applying a Tukey window before performing the fast Fourier transform (FFT). **a)** Properly windowed temporal waveform. **b)** Fourier transform of properly windowed temporal waveform. **c)** Improperly windowed temporal waveform, truncating the beginning of the pulse. **d)** Fourier transform of improperly windowed temporal waveform, displaying an artificially created DC offset.

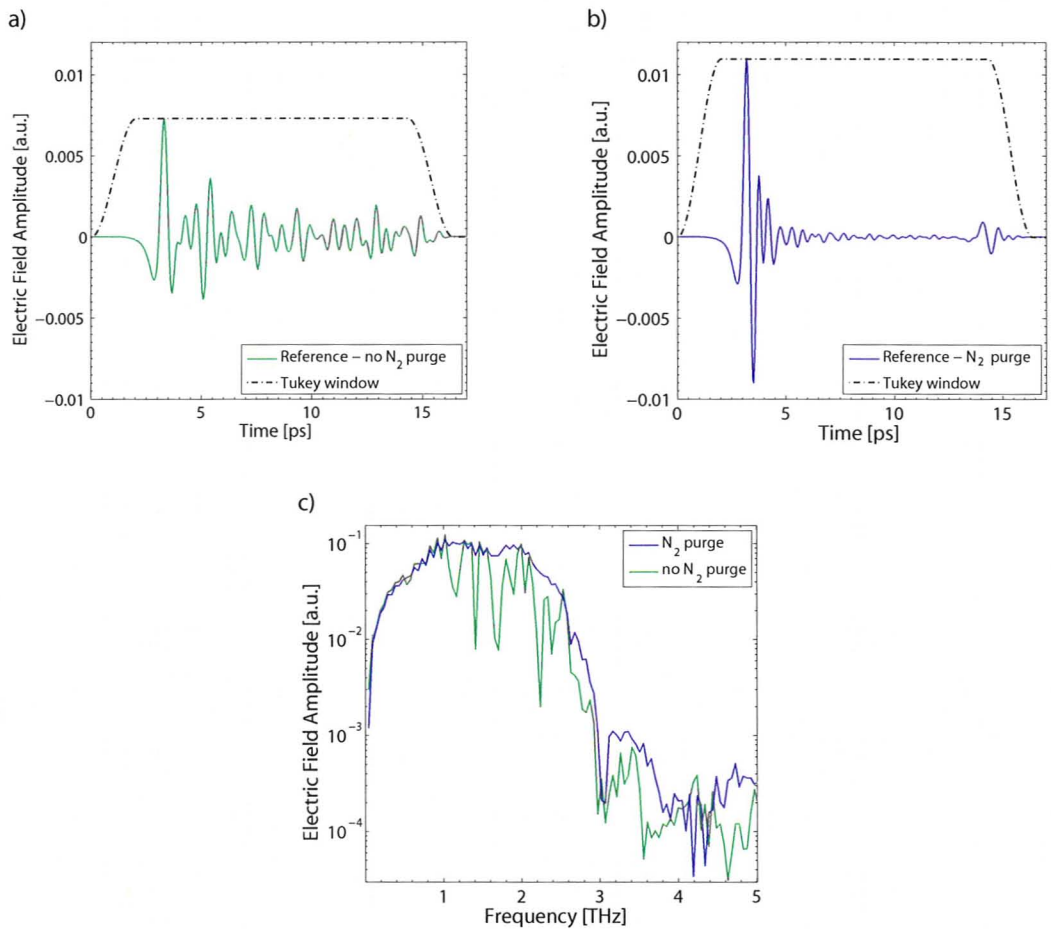

Figure 2.7: Transmission reference scans demonstrating the effects of water vapour in nitrogen (N_2) purged and unpurged conditions. A Tukey window is applied to the temporal waveform before performing the FFT. **a)** Plot of the temporal waveform of a THz pulse without N_2 purge. **b)** Plot of the temporal waveform of a THz pulse with N_2 purge. **c)** Fourier transform displaying broadband spectral information and the water absorption lines caused by water vapour.

ringing after the pulse due to the dispersion and absorption of the THz radiation by water vapour. In the frequency spectrum, the presence of water vapour exhibits itself as strong absorption lines [40]. When water vapour is purged from the THz beam line, the ringing, following the temporal waveform, is greatly reduced, yielding a much shorter THz pulse. In Fig. 2.7 b) a second THz pulse is observed approximately $\sim$10 ps after the main pulse. This echo pulse is caused by a reflection in the generator crystal.

Chapter 3

Experimental Setup

3.1 Ultrafast Laser System

A commercial Spectra Physics titanium:sapphire chirped-pulse amplifier (CPA) system is used to produce the ultrashort laser pulses required for the OR generation of THz radiation. This system has four primary elements: a Ti:sapphire oscillator and its pump laser, and a regenerative amplifier and its pump laser.

The Spectra-Physics Millennia V system [41] is a CW frequency doubled neodymium yttrium vanadate laser with an output wavelength of 532 nm. The Millennia produces 4.35 W of green light used to pump the Spectra-Physics Tsunami [42], a Ti:sapphire oscillator. The oscillator outputs pulses with a central wavelength of 800 nm at a repetition rate of 80 MHz. The duration of these pulses are optimally <50 fs, with a pulse energy of ~5.5 nJ and a bandwidth of roughly 50 nm. The pulses generated by the oscillator are then amplified using a Spectra-Physics Spitfire Ti:sapphire chirped-pulse amplifier [43], which is pumped by a Q-switched, frequency doubled, diode-pumped Nd:YLF Laser (Spectra-Physics Evolution [44]) operating at 527 nm with a power of approximately 5.25 W.

Attempting to amplify an ultrashort pulse directly would lead to a pulse with a peak intensity above the damage threshold of the optical components, as well as nonlinear effects during the amplification process. To avoid this problem of high instantaneous energy, the pulse is temporally stretched before amplification. The pulses are stretched with the use of a multi-pass, single grating configuration. In this

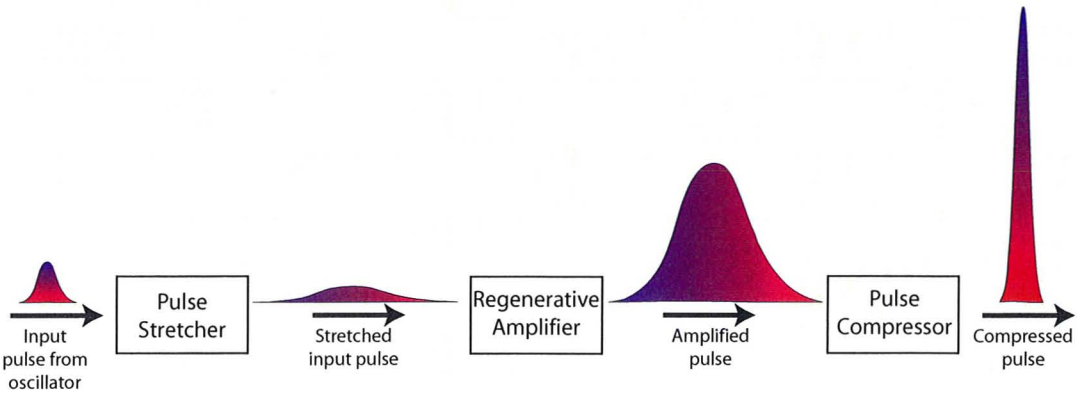

Figure 3.1: Simplified representation of the chirped-pulse amplification process [46].

configuration the spectral components of the incoming pulse are spatially separated, such that the different frequencies have different path lengths. When the components are recombined, the path length differences result in a temporal broadening of the pulse. Once the peak intensity of the pulse has been reduced to below the damage threshold of the optical components, the pulse is amplified in a multi-pass amplifier cavity. Following amplification, the pulse is compressed using a similar technique to the stretching process (see Fig. 3.1) [45]. Optimally, this would yield a pulse with a duration of ~50 fs and an energy of ~800 μJ at a repetition rate of 1 kHz.

3.2 THz Experimental Setup

In this setup THz radiation is generated via optical rectification in a ZnTe crystal and it is detected through electro-optic sampling (see Figs. 3.2-3.4).

The incoming 800 nm radiation is split into three beams: the majority is used for the generation of the THz radiation, ~1% acts as the probe for detecting the THz pulse, and ~20% is used as an optical pump for optical-pump, THz-probe experiments. The generation beam passes through a 300 μm thick, $\langle 1\ 1\ 0 \rangle$ oriented ZnTe crystal, generating THz radiation via OR. The THz beam is focused through a series of 90° off-axis parabolic mirrors onto a sample, and then refocused onto a second ZnTe crystal for detection. The linearly polarized probe is guided such that it collinearly propagates through the detector crystal with the THz radiation.

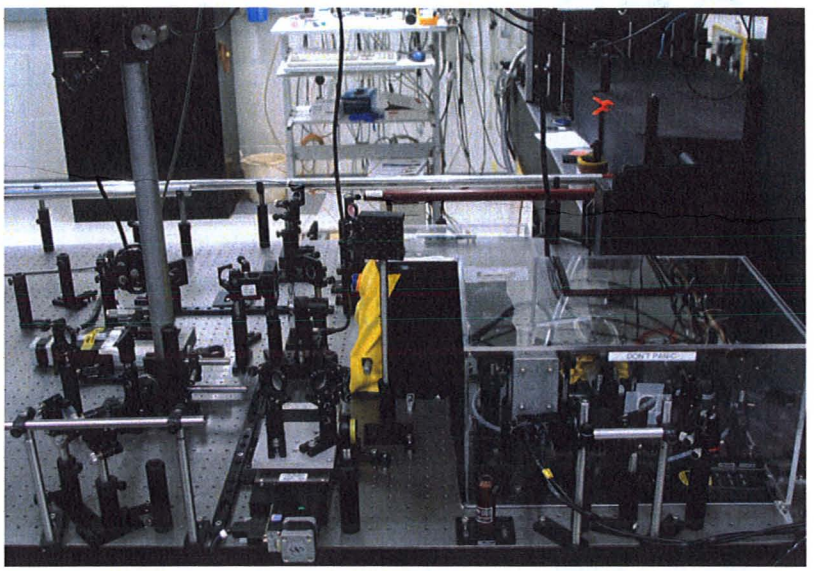

Figure 3.2: Photograph of the THz setup. THz generation and detection occurs within the plexiglass enclosure (see Fig. 3.3).

The detection line uses the ZnTe crystal and a $\lambda/4$ plate, which act as a variable wave plate [47]. In the absence of a THz beam, a linearly polarized probe pulse passes through this variable waveplate, yielding circularly polarized light. A Wollaston prism spatially splits the linear components of the circularly polarized probe beam into two equal intensity beams, which are then detected by balanced photodiode detectors. When the THz pulse is present it induces a weak birefringence in the ZnTe detector crystal which changes the polarization of the incoming probe pulse from linear to elliptical. The degree of ellipticity induced in the probe beam is proportional to the amplitude of the THz electric field that is incident on the detector crystal. This is detected as the difference in the photodiode signals. A delay stage in the THz generation beam line allows for the full THz wave form to be scanned through the probe pulse [48, 49]. The THz beam is chopped at half the repetition rate of the laser (i.e., if the laser is running at 1 kHz, the THz beam is chopped at 500 Hz). By using a lock-in amplifier to lock in to the reference signal from the chopper, the THz signal can be separated out from the probe pulse and noise.

Black polyethylene filters are placed in the collimated THz beam paths. Polyethylene is invisible to THz frequencies, however it effectively blocks any residual 800 nm

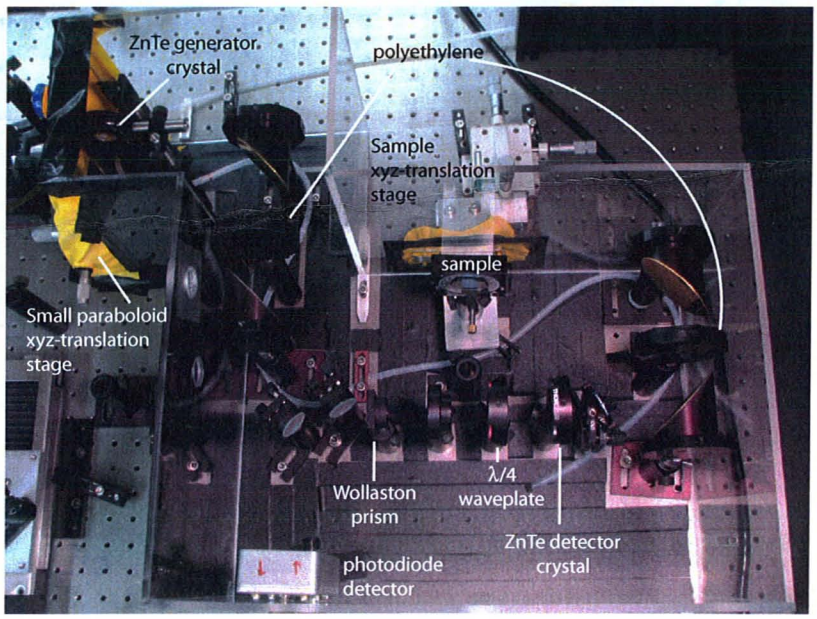

Figure 3.3: Photograph of THz beam line and detection line within the plexiglass enclosure.

light that passes through the ZnTe crystal. This filter serves two purposes: the chopped 800 nm light from the generation beam path could obscure the balance of the photodiode detectors, and, if the 800 nm light from the generation line were to propagate through the THz beam path, it would be focused down onto the detector crystal, potentially damaging it.

To aid with the alignment of the system when switching between transmission, reflection, and ATR geometries, the first small parabolic mirror is on xyz translation stages (see Fig. 3.3 and 3.4). When the aluminum reflector piece, used to switch the system to a reflection configuration, and the ATR prism are placed in the setup, the THz beam path is changed slightly and alters where the focus of the THz radiation is relative to the sample. Translating this parabolic mirror shifts the location of the THz focus on the sample and moves the THz image on the detector crystal. Adjusting the position of the THz focus is necessary when incorporating the reflector piece or ATR prism into the setup to ensure that the THz beam is as focused as possible when interacting with the sample.

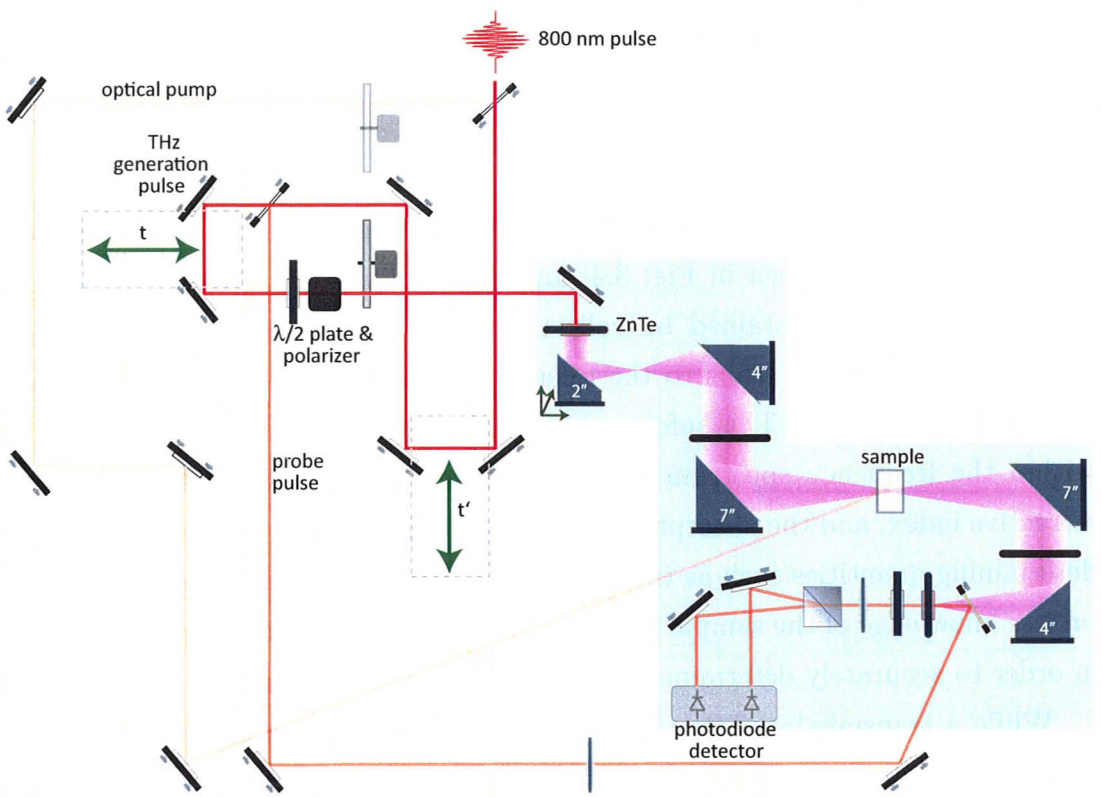

Figure 3.4: Schematic of the experimental THz setup. The focal lengths of the parabolic mirrors are denoted by the white numbers.

3.2.1 Plasma generation

To generate THz radiation with air plasma, minor modifications were made to the existing setup. By removing the ZnTe crystal, the 800 nm light is focused by the first parabolic mirror to create air plasma. To generate THz radiation with a plasma formed from both fundamental and second harmonic wavelengths, a β-barium borate (β-BBO) crystal was placed at the former location of the ZnTe crystal to convert some of the 800 nm light to 400 nm through SHG. In both generation schemes the detection method remained the same.

3.2.2 Transmission

In the transmission experimental setup, a sample is placed at the focus of the third parabolic mirror, as seen in Fig. 3.4, and THz radiation is transmitted through it. A reference scan is obtained by collecting data in the absence of a sample. By comparing the sample scans to the reference, the effect of the sample itself can be seen in the THz data. This information can be used to determine absorption peaks within the frequency spectrum of the generated and detected THz radiation, the refractive index, and the absorption coefficient of the sample. It should be noted that determining quantities such as the refractive index and absorption coefficient require precise knowledge of the sample thickness that the THz radiation propagates through in order to accurately determine the phase information required for this calculation.

While a transmission THz radiation experiment is commonly employed, not all samples are suitable for this method of examination. For this reason, the experimental setup is constructed in such a way to adopt other geometries which can accommodate samples that cannot be easily probed by the transmission of THz radiation.

3.2.3 Reflection

THz reflection spectroscopy is a more accommodating approach to examining liquid samples. Unlike transmission, this configuration does not require a thin fluid cell to examine strongly absorbing liquid samples. In order to create a reflection geometry for the THz setup, an aluminum reflector piece was manufactured to be placed near the THz focal point, where the sample would go in a transmission experiment (see

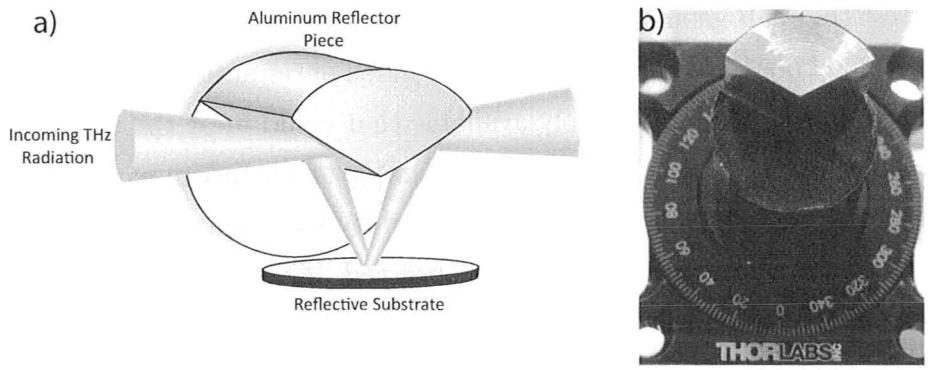

Figure 3.5: **a)** Schematic of the THz reflection geometry. **b)** Photograph of the reflector piece mounted on a rotation mount for ease of alignment. The reflector piece is machined from a solid aluminum rod, with an apex angle of 120°.

Fig. 3.5). The purpose of the aluminum reflector piece is to reflect the THz radiation down onto the sample and, once it has reflected off the sample, reflect the THz radiation back to the original THz beam path. While the surface of this prototype reflector piece is not polished to optical quality, it is presumed that this will not have a large effect on the reflected THz radiation as the wavelengths in the pulse are much greater than the surface roughness of the reflector piece.

The sample stage is a metallic mirror, which has xyz translation capabilities. To obtain a reference scan in the reflection configuration, the THz radiation is reflected off a bare metallic mirror. When scanning a sample, the sample is placed on the metallic mirror and the height of the sample stage must be adjusted to correct for the thickness of the sample, to maintain proper alignment of the THz beam.

3.2.4 Attenuated Total Reflection

Certain samples such as polar liquids, strongly absorbing samples, and powders, may be challenging to investigate using transmission. While it is possible to investigate liquids via reflection THz experiments, it can be difficult to extract information about the solute molecules in solutions because of the short interaction length [37]. Powders pose the additional complication that reflection off the sample results in a diffuse reflection, which weakens the signal. All of these factors make attenuated total reflection (ATR) a viable alternative.

To test the ATR geometry, without incurring any major expenses, a test prism was first machined out of teflon. Due to the low index of refraction of teflon (n ~1.44) [50], no trial samples were immediately available that could meet the total internal reflection requirements. However, by placing a sample on the prism with a higher than the maximum allowable refractive index dictated by the requirements for TIR, the destruction of the TIR condition could be observed. This greatly reduces the measured THz signal, as part of the THz radiation would be transmitted through the sample. The prism was machined from a 1" rod of teflon with an apex angle of 130°. The size and geometry of the prism was chosen to minimize the path length of the THz beam through the prism, while still having a reasonable sized surface on the prism for sample placement.

A number of different materials were considered for the ATR prism. Potential materials included TPX, Tsurupica, Si, Ge and MgO. Although materials like TPX and Tsurupica have high transmission in the THz frequencies, they, like other polymers, have relatively low refractive indices (n ~1.4). A low refractive index severely restricts the possible samples that can be examined, as the sample must have a sufficiently lower refractive index than the prism to satisfy the TIR condition.

For the purpose of investigating liquids, in particular water, which has a refractive index of ~2.6 - 1.8 in the range of 0.5 - 4 THz, Si (n ~3.42) [51] and MgO (n ~3.10) [50] were the most viable candidates. To minimize absorption in semiconductor-based prisms, the material needs to be of high purity and have sufficiently low defect density. For these reasons, high resistivity float zone (HRFZ) silicon was chosen for the prism material since it meets the above requirements and high purity custom Si optics were available through the company Tydex (see Fig. 3.6).

Four HRFZ Si prisms were purchased to allow for multiple types of THz ATR experiments. The Si prisms have an apex angle of 103° and a top surface that is 10 mm × 13 mm. This apex angle was chosen so that a horizontally propagating THz beam incident on the prism would satisfy the TIR condition when reflecting off the top surface if a sample with a refractive index of < 2.67 was placed on the prism (see Fig. 3.7). The apex angle for this configuration can be determined using the refractive index of the prism material and the refractive index of the desired sample.

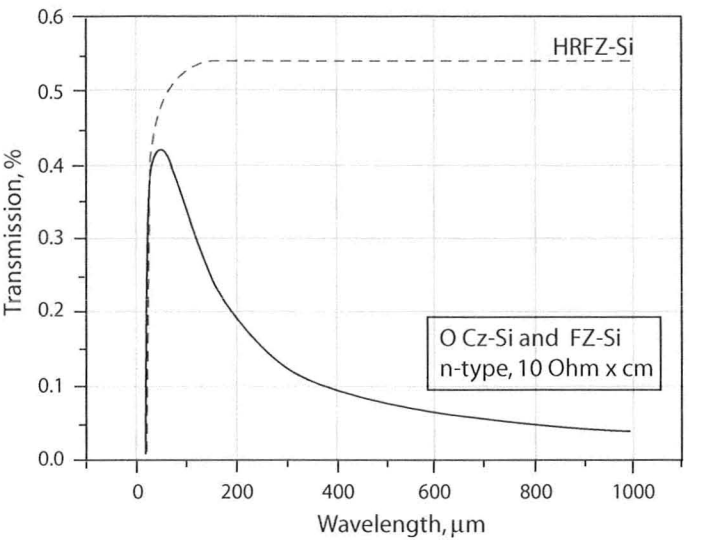

Figure 3.6: Si Transmission data, from 16 - 1000 μm, provided by Tydex [52]. This plot displays the difference in transmission of 5 mm thick samples of Optical Czochralski (OCz) Si and Float Zone (FZ) Si compared to High Resistivity Float Zone (HRFZ) Si in the far infrared spectrum.

Using Eq. 2.10 and Eq. 2.11, the relation to determine the apex angle is given by

$$\tan\phi = \frac{\sqrt{n_p^2 - n_s^2}}{(n_s - 1)}. \tag{3.1}$$

At the time, it seemed favourable to choose a geometry that would result in an angle of incidence close to the critical angle for TIR, while still being greater than it, in order to maximize the penetration depth of the evanescent wave. In hindsight, however, it may have been advantageous to choose an slightly larger angle. While this would have reduced the penetration depth, effectively reducing the signal, it would have also given a little more leeway with the incident angle, ensuring that the TIR conditions were not violated.

The overall size of the prism was decided such that the prism would be large enough to accommodate a fluid cell, while still being small enough to avoid large changes in the optical path length. Because of the high refractive index of Si in the THz regime, the prism lengthened the optical path length by ~20 mm. While this would shift the focus of the THz beam, large effects were not anticipated because of

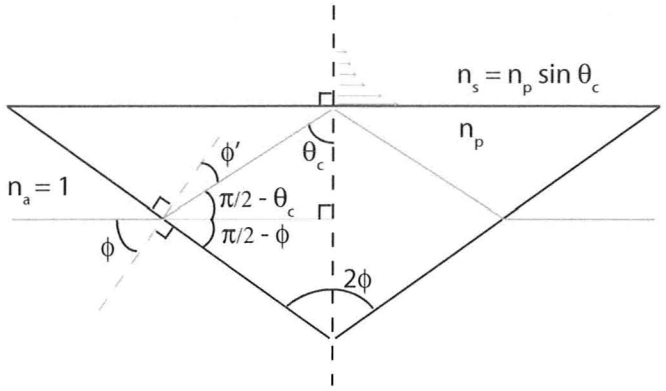

Figure 3.7: Geometric relations considered when choosing the apex angle of the prism.

the long focal length of the 7" parabolic mirrors coupled with the alignment adjusting capabilities of the 2" parabolic mirror.

One of the Si prisms was modified to accommodate liquid samples. A 15 mm tall glass tube with a diameter of 10 mm was fixed to the surface of the prism using crystal bond (see Fig. 3.8). When performing experiments with this fluid cell a rubber stopper was placed over the opening of the glass tube to prevent evaporation of the sample and, for the case of water, to minimize the water vapour in the N_2 purged plexiglass enclosure.

As the effective thickness of the evanescent wave electric field propagating into the material is greater for p-polarized light than s-polarized light (refer to Eq. 2.17 and Eq. 2.18), it was favourable to generate vertically polarized THz radiation to maximize the interaction of the THz radiation with the sample. This was achieved by generating THz pulses with vertically polarized 800 nm pulses and adjusting the orientation of the ZnTe generator crystal to maximize THz beam power. Since the laser generates horizontally polarized 800 nm pulses, a half wave plate and polarizing beam cube were placed in the THz generation beam line before the ZnTe generator crystal. Incorporating these optical components into the setup facillitated the switch between horizontal and vertical polarizations.

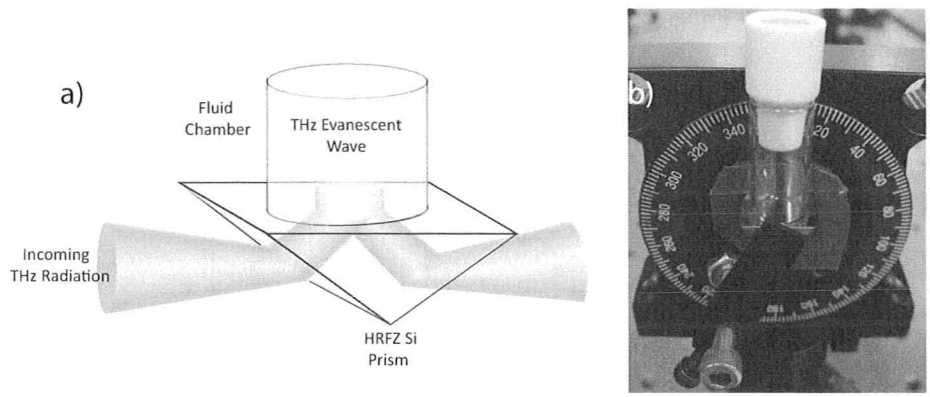

Figure 3.8: **a)** Schematic representation of the THz attenuated total reflection (ATR) geometry. **b)** Photograph of the ATR prism with fluid cell mounted on a rotation mount for ease of alignment. The prism is composed of high resistivity float zone silicon and has a refractive index of n=3.42 at THz frequencies.

3.2.5 Optical-Pump, THz-Probe

A pump beam is split off from the incoming 800 nm beam using a 20% beam splitter, as shown in Fig. 3.4. This is used to optically excite the sample in the various experimental setup geometries. The pump beam path has to be precisely the same length as the THz generation beam path so the optical excitation pulse and the THz pulse reach the sample at the same time. The relative delay between the pump beam and the THz pulse is controlled by a delay stage which scans both the THz generation line and the optical probe through the optical excitation pulse. Holding the optical probe fixed in time while the THz pulse is scanned enables the examination of a specific point in time following the optical excitation, as shown in Fig. 3.9. The chopper is moved to the pump beam path such that the lock-in amplifier detects the change in the THz signal as a result of the sample being pumped. Unfortunately, the length of the delay stage used for these experiments was limited to 666 ps, making it difficult to accurately examine samples with a long carrier lifetime.

3.2.6 Experimental Obstacles

This section addresses some common experimental issues that require attention when performing THz TDS.

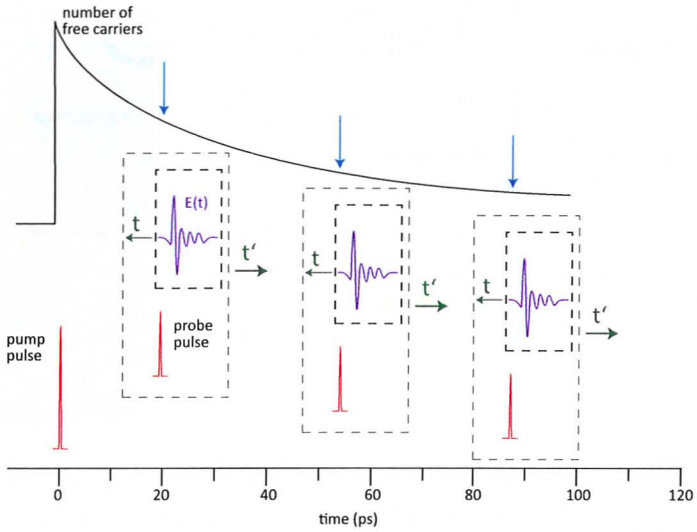

Figure 3.9: This plot displays the pump-probe scanning processes. At various times after the optical pump excitation (indicated by the blue arrows), the optical probe pulse is held fixed while the THz pulse is scanned through it. By monitoring the changes in the THz wave form at different pump times, free carrier relaxation can be observed.

The generated THz pulses contain a broad range of frequencies, leading to problems when focusing the THz beam onto the detector crystal. High frequencies focus more tightly than low frequencies (see Fig. 3.10). Therefore, when the THz beam is focused it results in a relatively large spot size, however only the central region of the spot contains both high and low THz frequencies. When dealing with the alignment of the THz beam and the 800 nm probe pulse on the detector crystal it is crucial that the probe pulse spot completely overlap the THz spot on the ZnTe detector crystal in order to retain broad bandwidth information. If the probe and THz spots are not centered on each other, high frequency THz radiation information can be lost.

Another experimental obstacle when working with THz radiation is the effect of humidity. Water vapour is a strong absorber of THz radiation [40] leading to complications when performing THz experiments in ambient air. Depending on the humidity level throughout the course of an experiment, absorption of water vapour can cause issues of phase shift between scans, due to the change in effective path length as a result of refractive index fluctuations of the air. The spectroscopic data

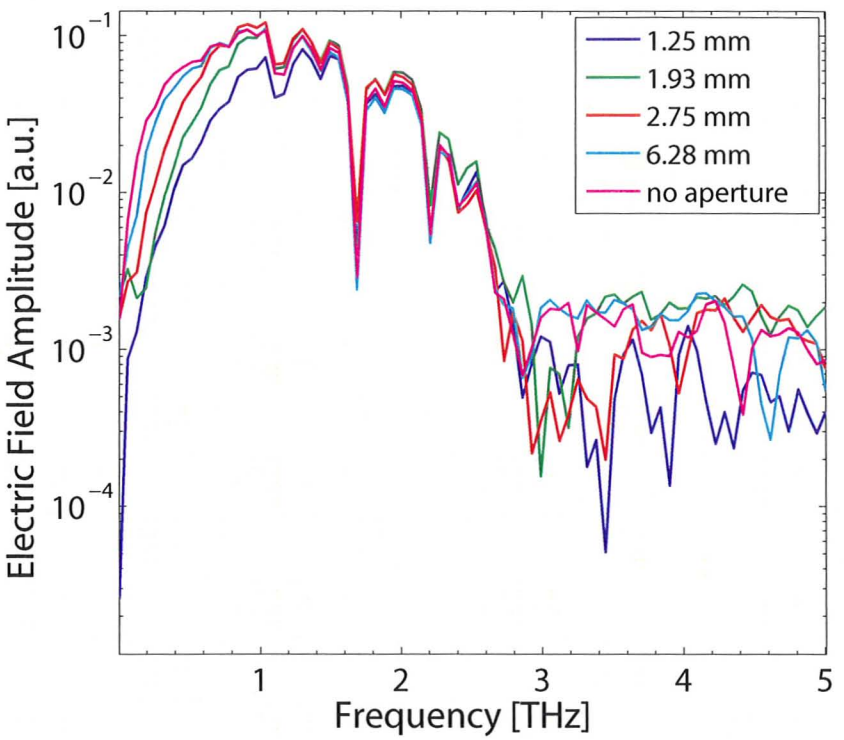

Figure 3.10: THz frequency spectrum obtained under unpurged conditions for varied aperture sizes at the THz focus. As the aperture is closed, low frequency information is reduced while the high frequencies remain relatively unaffected. Data courtesy of Derek Sahota and Zach Watling.

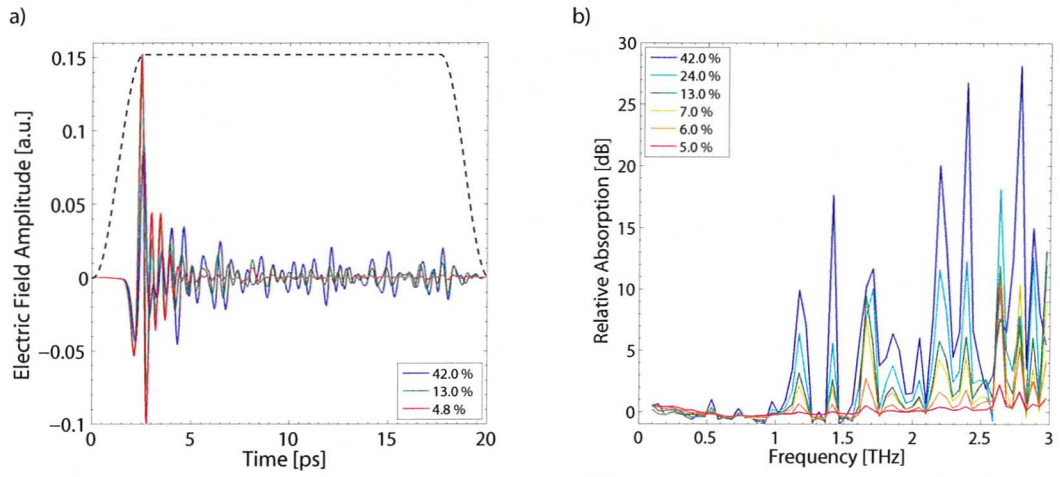

Figure 3.11: **a)** THz temporal waveform displaying change in the amplitude and pulse duration as humidity is altered. **b)** Water absorption peaks in the THz spectrum. Data and analysis courtesy of Derek Sahota.

collected in humid conditions can be problematic because of the strong water vapour absorption lines, as can be seen in Fig 3.11. To remedy this issue, a plexiglass box was constructed to enclose the entire THz beam path, which can be purged with dry nitrogen (Fig. 3.2). A psychrometer is placed in the purge box to monitor the humidity level throughout the course of an experiment.

Noise was another reoccurring experimental concern. A periodic noise signal was often observed that was thought to be caused by the vibration of the pellicle beam splitter. It is speculated that the resonance frequency of the pellicle is close to ~500 Hz. When the laser is operating at a 1 kHz repetition rate, the THz radiation is also being sampled at 500 Hz, making the resonance of the pellicle highly noticeable. There are two options available to deal with this particular situation. The pellicle beam splitter could be replaced with one of a different size, which would subsequently have a different resonance frequency, or the repetition rate of the laser could be changed such that the sampling rate of the THz pulse is a little further away from the pellicle resonance frequency. The latter was chosen and the laser was operated at 1.1 kHz, to give a THz sampling rate of 550 Hz.

Chapter 4

Early Exploratory Experiments

4.1 Plasma THz Generation

The generation of THz radiation from air plasma was a technique that was briefly explored. In the preliminary experiment this method of generation resulted in a much weaker THz pulse, approximately 230× weaker than the OR generated pulse. The generation efficiency was improved by using both fundamental and second harmonic spectral components to create the plasma. A β-BBO crystal was required for second harmonic generation. Using both 800 nm and 400 nm light to generate the plasma yielded a THz pulse that was only 35× weaker than the OR generated pulse (see Fig. 4.1).

The result presented in this section was the first attempt of generating THz radiation with an air plasma. If this technique were properly optimized, it could provide an alternative to THz generation via optical rectification. However, for this to be a competitive alternative, it would most likely require an upgraded amplification system to increase the intensity of the laser pulse used to generate the plasma. Before resorting to a system upgrade, there are other approaches that may be considered to improve the efficiency of generation. Obviously the minimization of water vapour in the THz beam line requires the systems environment to be purged with some sort of dry gas. Nitrogen was used as the purge gas for this experiment, however different gases may yield more favourable results [53]. Improving the efficiency of the 2^{nd} harmonic generated 400 nm light, as well as applying an external DC field to the region

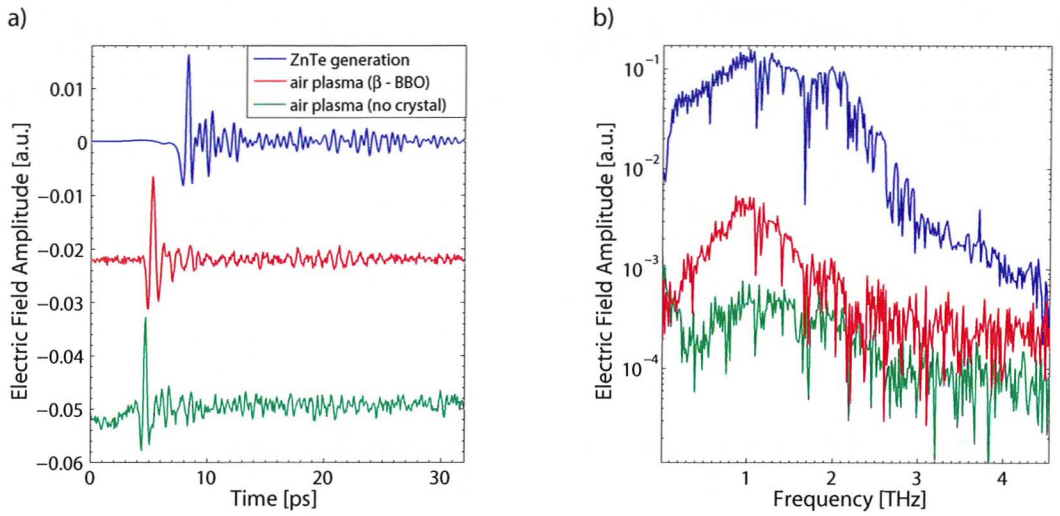

Figure 4.1: THz generation via OR and N_2 plasma THz generation are compared. (N_2 purge not optimized.) **a)** Temporal waveforms of THz pulses generated by OR in a ZnTe crystal, N_2 plasma THz generation via FWR ($\times 35$), and N_2 plasma THz generation with no crystal present ($\times 230$). The data is offset for clarity. **b)** Fourier transforms displaying frequency bandwidth and noise level of each method

of the plasma, are also methods of increasing THz pulse amplitude [19].

4.2 Transmission and Reflection THz Measurements of Polymer Films

This section presents preliminary data on transmission and reflection THz spectroscopy of polymer films. The study of polymer systems is a rapidly growing and important area of physics. An effort was made to explore how THz based studies might be used in this area, thus contributing to a field that is already very actively pursued in the departments of physics and chemistry at McMaster University. The samples, various thicknesses of polystyrene films spin-coated onto silicon substrates, were prepared by Josh McGraw from the Experimental Polymer Physics Group. Prior to examining the polystyrene films, plastic film (saran wrap) was first examined in transmission and reflection mode as a crude method to test the possibility of using THz radiation to detect polymer films.

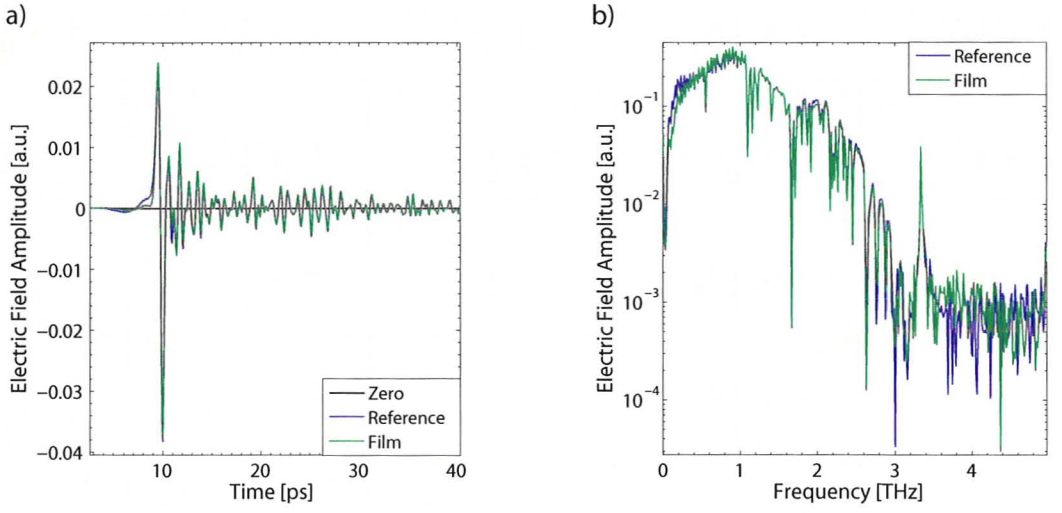

Figure 4.2: Transmission THz spectroscopic results for saran wrap. (No N_2 purge.) **a)** Temporal waveform of the reference scan and scan with saran wrap present in the beam line. **b)** Fourier transform of the temporal waveforms.

In the transmission experiment, the film was mounted on a 2" lens mount such that the film was taut but not distorted or deformed from the tension. It was placed in the sample position at the focus of the THz beam path (see Fig. 3.4). A reference scan was obtained by performing a scan with no sample present. Fig. 4.2 presents the results.

In the reflection experiment, we obtain a reference scan by placing a metallic mirror on the sample stage. The saran wrap was first measured by placing it over top of this metallic mirror, and secondly as a free standing film with no metallic mirror below (Fig. 4.3).

Three thicknesses (~35 nm, ~105 nm, and ~165 nm) of polystyrene film on ~1 cm^2, ~500 μm thick silicon substrates were examined in transmission mode. The samples were placed at the focus of the THz beam in the sample position such that the THz pulse would be incident on the polystyrene film. Two different reference scans were obtained to compare to the sample: a standard reference with nothing present in the THz beam line, and a substrate reference with a blank Si substrate placed at the focus of the THz beam. With regards to the substrate reference, the Si wafer was placed in the beam line such that the THz pulse was incident on the polished side of the wafer. There is a temporal shift between the reference scan and

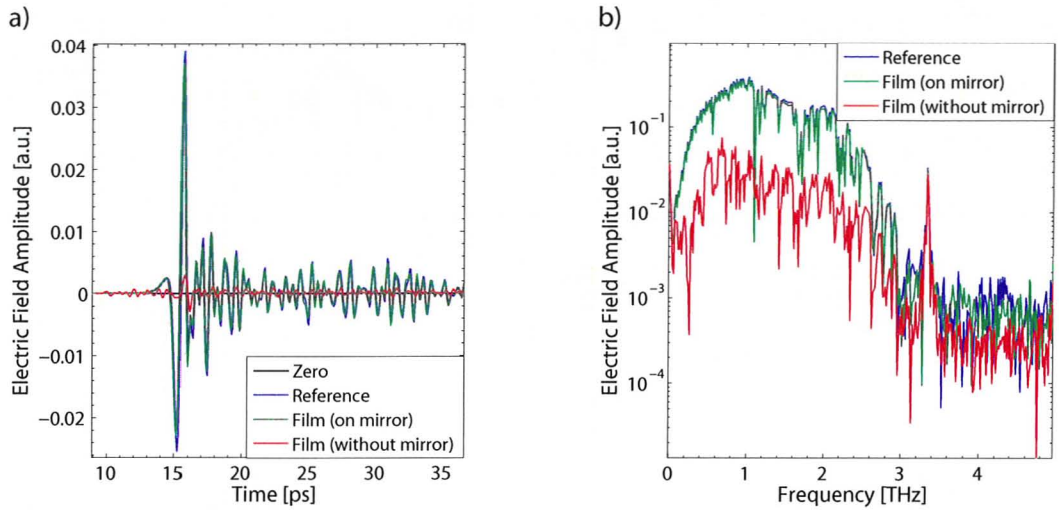

Figure 4.3: Reflection THz spectroscopic results for saran wrap. (No N_2 purge.) **a)** Temporal waveform of the reference scan, scan with saran wrap present on the metallic mirror, and scan of the saran wrap with no metallic mirror. **b)** Fourier transform of the temporal waveforms.

the "reference" of the blank substrate. The finite thickness of the silicon wafer creates a difference in the optical path length of the THz pulse between the two references. The THz signal from the substrate with polystyrene film was greatly reduced to the point of not being discernible from the noise level. It is speculated that this may be a result of the difference in the Si wafer substrates. The substrates that the samples were spin-coated on to were not cleaved from the same wafer as the blank substrate that was examined. This could be problematic because, while silicon does not absorb THz radiation, any impurities or defects in the silicon can strongly absorb. Since these samples were prepared with the intent of creating a high quality thin-film, the only concern was the surface quality of the silicon wafer, not the quality of the bulk silicon itself for THz applications (see Fig. 4.4).

The polystyrene films were also examined in reflection mode (see Fig. 4.5). The samples, including the blanks substrate, were placed on the metallic mirror. The sample stage was translated in the z-direction to offset the thickness of the substrate. From the results presented, it is unclear as to how effective THz radiation is as a probe for examining thin films. Although a difference between the spin-coated and the blank substrate can be detected, the thicknesses of the films were not evident

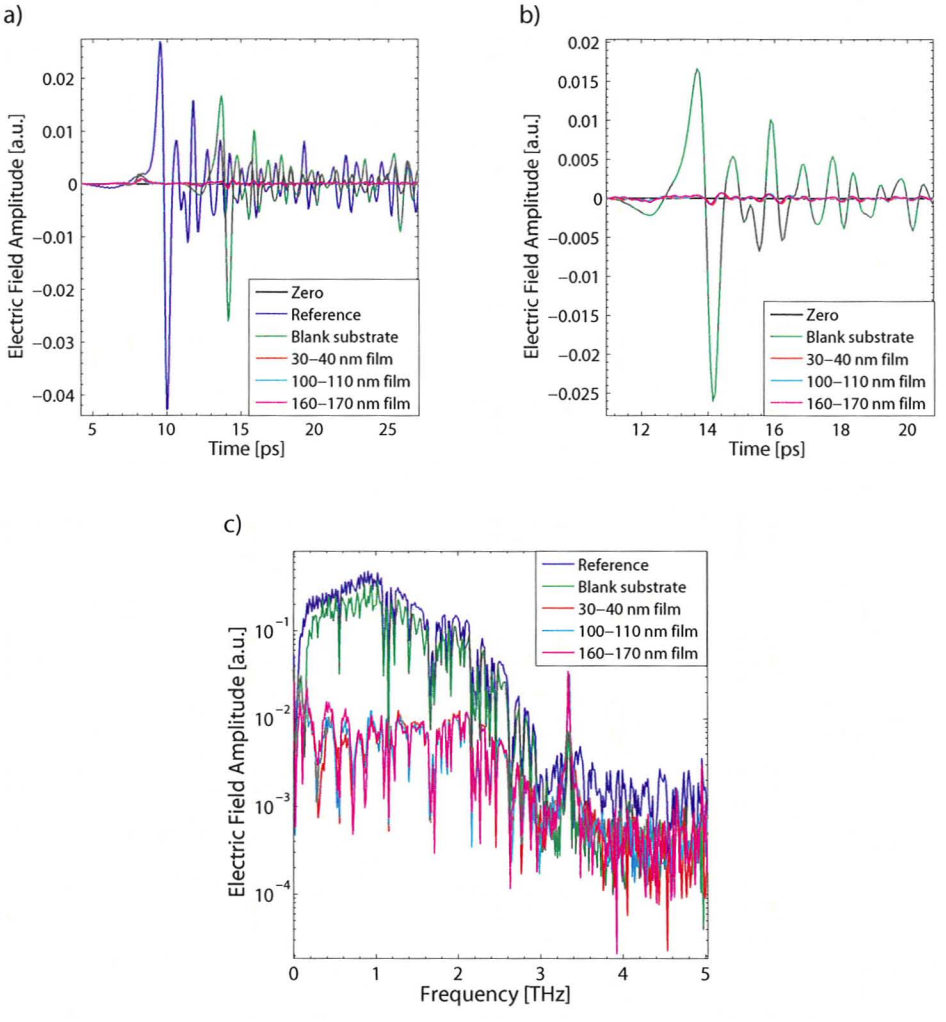

Figure 4.4: Transmission THz spectroscopy of polystyrene film on Si wafer. (No N_2 purge.) **a)** Temporal waveform of the reference scan, blank silicon substrate, and the polystyrene films on silicon substrate. **b)** Temporal waveform of just the blank silicon substrate and the polystyrene films on silicon substrate. **c)** Fourier transform of the temporal waveforms.

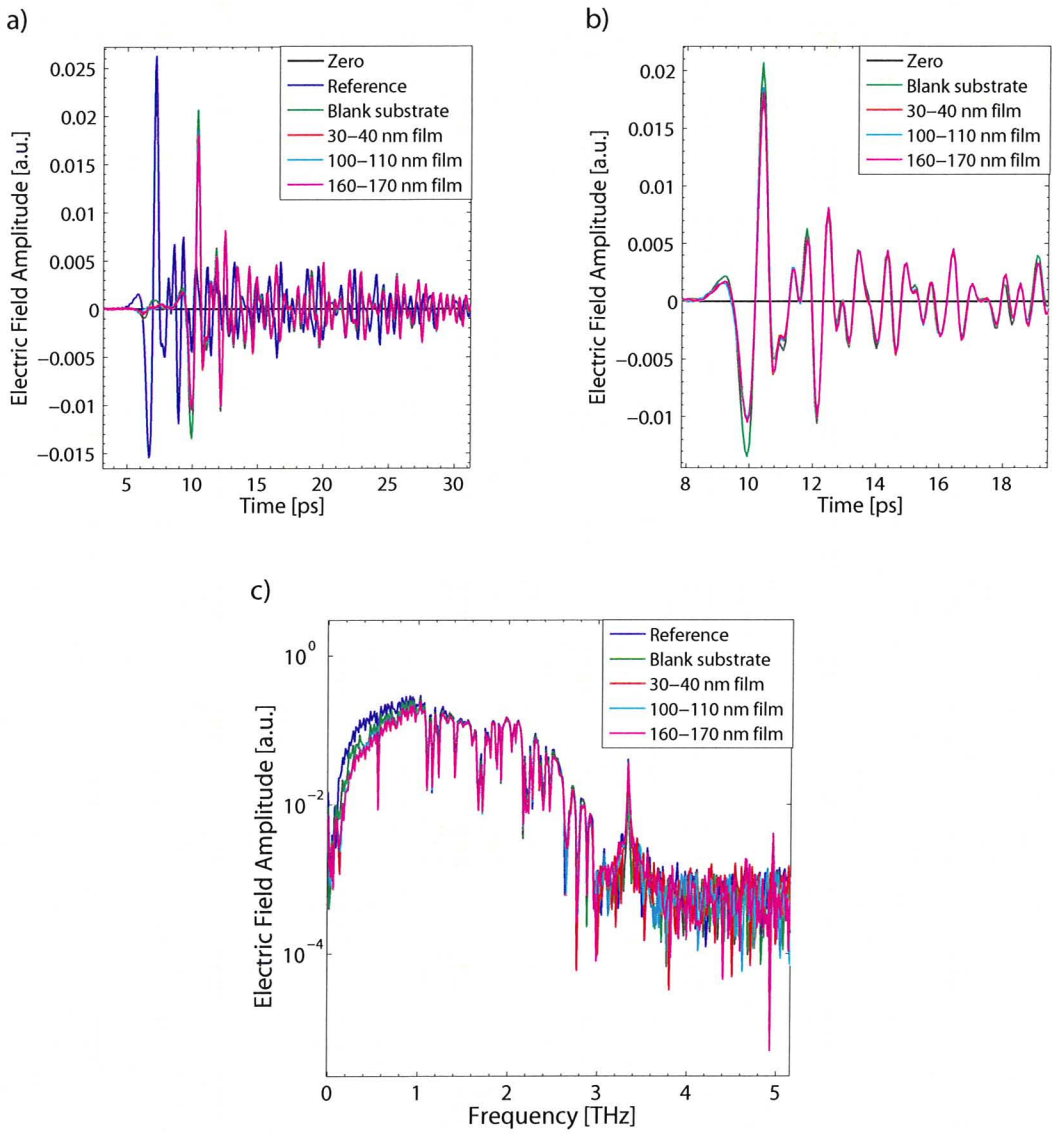

Figure 4.5: Reflection THz spectroscopy of polystyrene film on Si wafer. (No N_2 purge.) **a)** Temporal waveform of the reference scan, blank silicon substrate, and the polystyrene films on silicon substrate. **b)** Temporal waveform of just the blank silicon substrate and the polystyrene films on silicon substrate. **c)** Fourier transform of the temporal waveforms.

from examining the data. THz radiation may not have the required spatial sensitivity to accommodate thin films, with thicknesses that are substantially less than the wavelength of the THz radiation. For instance, the films examined in this experiment ranged from ~30 - 170 nm, while the wavelength at 1 THz is 300 μm. However, if one were to try and examine thin films spin-coated onto silicon substrates using transmission or reflection methods, the substrate itself would have to be well characterized first, and would optimally be high quality and high purity to minimize absorption from the substrate. Another technique that may yield the sensitivity required for this experiment would be to examine the thin film using attenuated total reflection techniques.

Chapter 5

THz Attenuated Total Reflection

While transmission and reflection based THz experiments allow for the investigation of a variety of materials, there are certain samples, such as powders and polar liquids, which yield less than favourable results. In transmission, powders pose the challenge of fabricating a thin free-standing sample, and strongly absorbing fluids, such as polar liquids, prove to be difficult to examine as they require the construction of a very thin fluid cell. Both of these samples have the additional complication that, because they are required to be so thin, they will inevitably produce weak THz signals as the THz radiation is interacting with very little material. Powders are also not suitable for examination in a reflection geometry as they cause diffuse reflection, resulting in a weak THz signal. These problems can be remedied by adopting an attenuated total reflection (ATR) configuration. Similar quality spectra to transmission can be obtained without the sample constraints. An additional advantage is that a reference scan can be obtained without altering the optical pathway of the THz radiation, since the sample is simply placed on the surface of the prism. This can allow for the evaluation of the complex dielectric constant, refractive index, and absorption coefficient of the sample.

5.1 Diagnostics and Results

5.1.1 Measurements using a Teflon Prism

A teflon prism was machined to test the geometry of the ATR experimental setup. While no samples were immediately available that would satisfy the TIR condition, a higher index material could be placed on the prism to destroy TIR, thus greatly reducing the THz signal. For convenience, the sample chosen was a commercially purchased, polymer based adhesive (sticky tac). Because the refractive index for teflon is approximately 1.44, the geometry of this particular prism allows for samples with refractive indices of < 1.3. As sticky tac is a polymer based substance, it is assumed to have a similar refractive index as other polymers (i.e. $\sim$1.4); therefore it is unlikely to satisfy the TIR condition.

A reference was obtained by collecting data with no sample present on the prism surface. Following the reference scan, sticky tac was placed on the surface of the prism. Fig. 5.1 demonstrates the importance of maximal contact between the sample and the prism surface. Once mild pressure was applied to the sample to ensure proper contact was established, the THz signal greatly decreased because of the partial transmission that would occur as the refractive index of the sample does not meet the conditions for TIR.

5.1.2 THz ATR of Solvents: Water, Methanol, and Ethanol

Biological samples require the understanding of how THz radiation interacts with liquid water in order to extract information about vibrational modes of molecules in solution in subsequent analysis. Water, ethanol and methanol were chosen as benchmarks liquids, as they have been previously examined via THz ATR [50, 51, 54]. Achieving expected results with these samples was necessary to ensure that the newly constructed setup was working properly.

Preliminary results show that water, methanol and ethanol can be differentiated

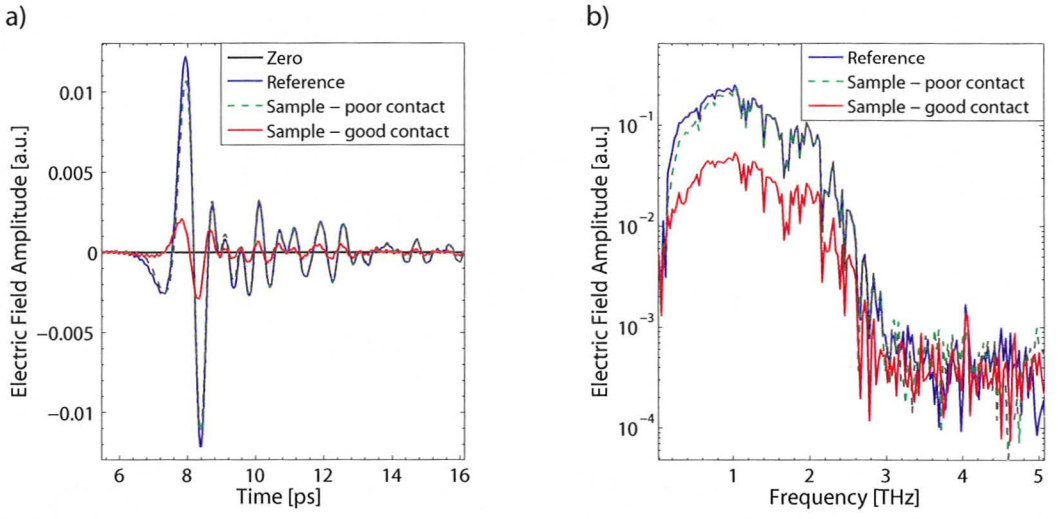

Figure 5.1: ATR using a teflon prism. **a)** Temporal waveform of the reference scan and sample scans under conditions of good and poor contact with the surface of the prism. **b)** Fourier transform of the temporal waveforms.

based on the ATR signal and relative phase ($\Delta\phi$) obtained.

$$ATR = \left| \frac{E(\omega)_{sample}}{E(\omega)_{reference}} \right|^2 \tag{5.1}$$

$$\Delta\phi = Arg \left[\frac{E(\omega)_{sample}}{E(\omega)_{reference}} \right] \tag{5.2}$$

$E(\omega)_{sample}$ and $E(\omega)_{reference}$ refer to the resultant electric field from the respective sample and reference scans. The comparison of these solvents is displayed in Fig. 5.2.

5.1.3 THz ATR of Water

Following the preliminary efforts with solvents, focus was shifted to the analysis of water. The signal-to-noise ratio was improved by averaging multiple THz scans of the sample. Reference scans were taken periodically between sample scans to ensure that the long term instability of the laser system was not prevalent, as a single scan takes up to 20 minutes. Fig. 5.3 shows that there is no overwhelming laser drift over time

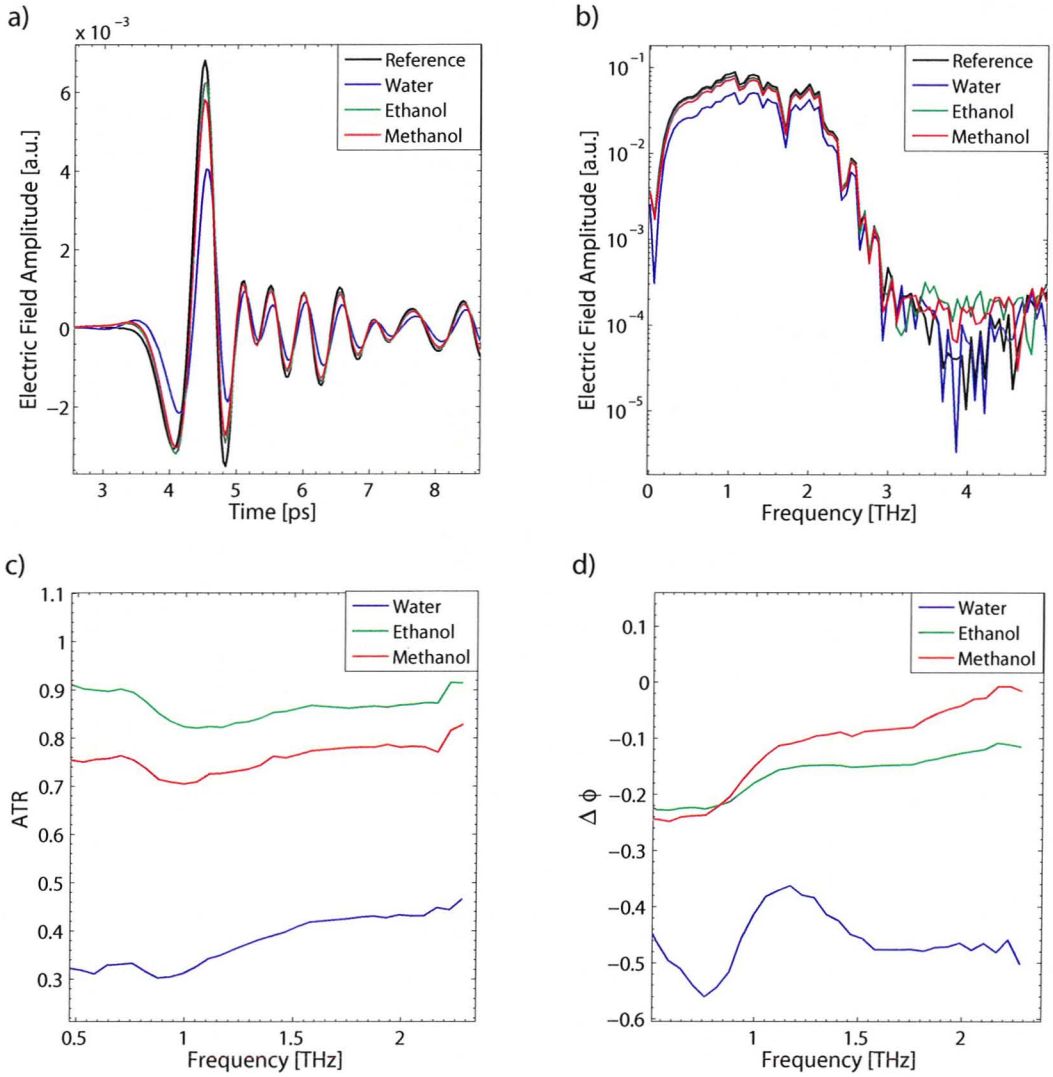

Figure 5.2: Experimental ATR data for water, methanol, and ethanol. **a)** Temporal waveform of the reference scan and solvent scans. **b)** Fourier transform of the temporal waveforms displaying the spectra of the solvents. **c)** ATR data obtained using Eq. 5.1. **d)** Relative phase data obtained using Eq. 5.2.

in both the sample and the reference scans, making them suitable to be averaged. The Fresnel reflection coefficients for the Si prism with and without a sample on the surface are given in Eq. 5.3a and Eq. 5.3b, respectively, where E_i and E_r are the incident and reflected electric fields. These equations can be combined to eliminate the dependence on the incident electric field, yielding an expression for the reflection coefficient in the presence of the sample (Eq. 5.4).

$$r = \frac{E_r}{E_i} \tag{5.3a}$$

$$r' = \frac{E_{r'}}{E_i} \tag{5.3b}$$

$$r = \frac{E_r}{E_{r'}} r' \tag{5.4}$$

The Fresnel equation for p-polarized light [36] in terms of the refractive index of the prism, n_1, and sample, n_2, and the angle of incidence θ is given by:

$$r_p = \frac{n_1\sqrt{1-(n_1/n_2)^2\sin^2\theta} - n_2\cos\theta}{n_1\sqrt{1-(n_1/n_2)^2\sin^2\theta} + n_2\cos\theta}. \tag{5.5}$$

r' can be calculated from the reference scan where the "sample" is simply air, therefore $n_2 = 1$. From this it can be shown that $r' = e^{i0.15}$. Rearranging Eq. 5.5, the complex dielectric function of the sample can be determined:

$$\varepsilon_{2\pm} = n_2^2 = n_1^2\left[\frac{(r-1)^2 \pm \sqrt{(r-1)^4 - (r-1)^2(r+1)^2\sin^2 2\theta}}{2(r+1)^2\cos^2\theta}\right], \tag{5.6}$$

where r is experimentally calculated using Eq. 5.4. From the complex dielectric function, the index of refraction, n, and the extinction coefficient, κ, of the sample can be extracted:

$$\sqrt{\varepsilon} = \tilde{n} = n + i\kappa, \tag{5.7}$$

$$n = \frac{\sqrt{\varepsilon_r^2 + \varepsilon_i^2} + \varepsilon_r}{2}, \qquad \text{and} \tag{5.8}$$

$$\kappa = \frac{\sqrt{\varepsilon_r^2 + \varepsilon_i^2} - \varepsilon_r}{2}, \tag{5.9}$$

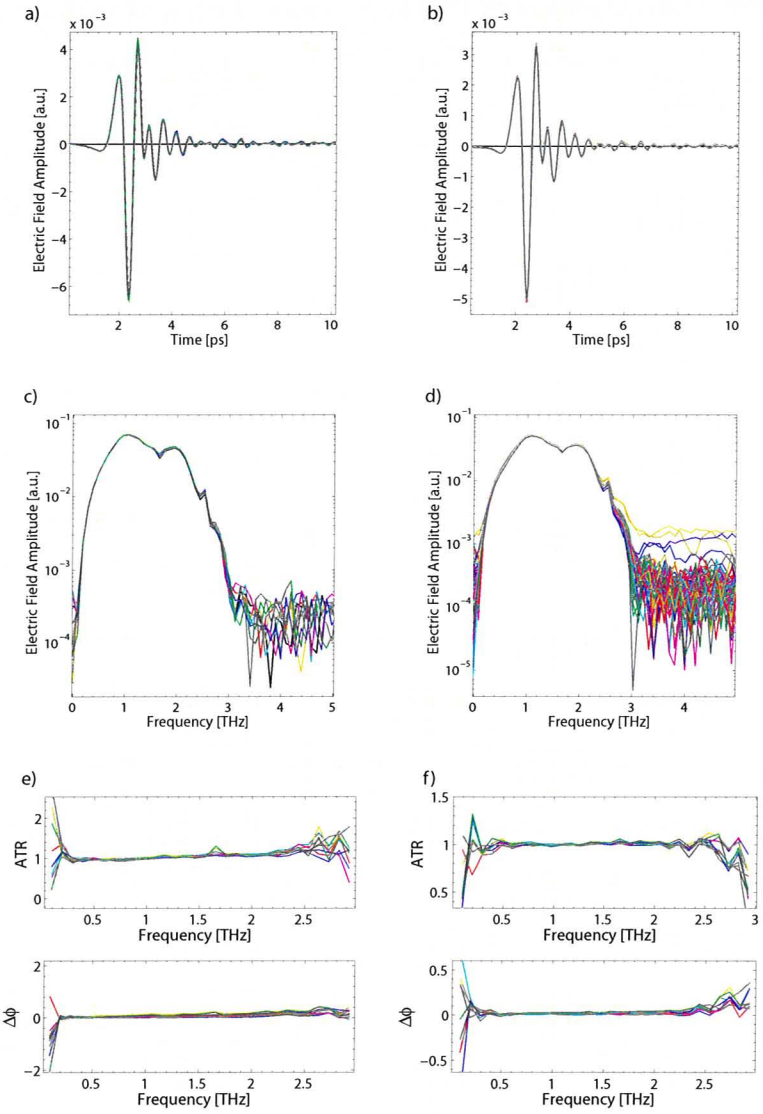

Figure 5.3: Reference [a),c),e)] and sample[b),d),f)] scans taken throughout the experiment, showing no significant changes over the course of the experiment. **a)** and **b)** Temporal waveforms. **c)** and **d)** Fourier transforms of the temporal waveforms. **e)** ATR data using the first reference scan (before any water has been introduced to the sample chamber) as the "reference" and the relative phase ($\Delta\phi$) between the reference scans. **f)** ATR data using the first sample scan as the "reference" and the relative phase ($\Delta\phi$) between samples scans. (Note that the expression for the ATR relation is given by Eq. 5.1 and relative phase by Eq. 5.2).

where ε_r and ε_i are the real and imaginary components of the dielectric function, respectively.

The aforementioned analysis was used to experimentally determine the refractive index and the extinction coefficient of water in the range of 0.5-2.5 THz. This calculation closely follows the analysis performed by Nagai *et al.* [51], however, suitable corrections were made to the equation for the dielectric function presented in the literature. There is an obvious absorption of THz radiation when water is present on the surface of the prism, as can be seen from Fig. 5.4 a) and b). Unlike with water vapour, this is a broad absorption over the entire spectrum. There are no sharp spectral absorption lines. Fig. 5.4 c) and d) show the ATR and relative phase data determined from Eq. 5.1 and Eq. 5.2. The calculated real and imaginary components of both roots of the dielectric function are shown in Fig. B.1 a).

The refractive index as a function of frequency, determined using this method (see Fig. B.1 b)), gave results much lower than the accepted values in this frequency range [55]. While there maybe multiple sources leading to this inconsistency, the mixed polarization of the generated THz radiation is a large contributing factor. Although efforts were made to ensure that the THz pulse that was generated was vertically polarized, upon closer examination, it is unclear as to how linearly polarized the generated THz pulses were. This is problematic because our method of analysis relies on the fact that we are using exclusively p-polarized light. When s-polarized light is used, the effective thickness of the evanescent wave is less than with p-polarized light (see Fig. 2.4). If a mixed polarization of THz radiation were used, it would reduce the evanescent wave effective thickness through the sample, artificially making the index of refraction (n) seem lower. This may account for the fact that the THz signal observed was not as strongly attenuated as results presented by Nagai [51].

The act of generating pure linearly polarized THz radiation is non-trivial. It is possible that the generated THz radiation may be interacting with the ZnTe generator crystal, causing an ellipticity in the tailing portion of the 800 nm generator pulse. This overall process can result in elliptically polarized THz radiation. These effects can be reduced by changing the crystal orientation; however a more optimal approach may be to use a THz polarizer following the generator ZnTe crystal. Unfortunately, THz polarizers are still in a developmental stage and tend to be both costly and have

questionable efficiency.

The polarization of the generated THz radiation was tested by examining the electric field amplitude as a function of generator and detector crystal orientation. By holding the angle of the generator crystal fixed and performing a full rotation of the detector crystal, the electric field amplitude can be mapped out. Comparing the measured electric field amplitude, as a function of detector crystal angle, to the theoretical electric field amplitude, under conditions of optimized generator crystal angle, allows one to determine the optimal generator crystal angle which maximizes the THz radiation output [32, 56]. To accurately map out the generator and detector crystal requires a time consuming iterative process. This process could be made more efficient with the use of motorized rotation mounts for both the generator and detector crystals. The preliminary calculation of the corrected generator crystal angle was done manually, in the absence of motorized rotation mounts, and should, therefore, only be considered a first approximation. The analysis software for undertaking this calculation was written by Derek Sahota, and it determined that, for optimal generation of THz radiation, the generator crystal was off by an angle of $\sim 15°$. Since the generator crystal was not optimally oriented for the experiment, the ellipticity of the generated THz radiation was not minimized. As the THz pulse incident on the prism was not purely vertically (p) polarized, using Eq. 5.5 to calculate the dielectric function, and subsequent optical properties, is no longer accurate.

Upon further consideration of the measurement of the optimal generator crystal angle, it was realized that the degree of ellipticity of the generated THz pulse could not be accurately quantified because of complications in the THz polarization measurement. During the initial alignment of the system it was ensured that the THz spot on the detector crystal overlaps the probe spot. However, if the 800 nm light is not centered on the ZnTe generator crystal initially, when the generator crystal undergoes a rotation to be optimized, the rotation of the generator crystal can walk the THz spot on the detector crystal off the 800 nm pump spot. In addition to this, there are slightly damaged regions on the detector crystal that was used. While the initial alignment may have been using an undamaged portion of the crystal, throughout the polarization test procedure it is possible that the measurement of the THz pulse was obscured because the THz and probe pulses were passing through damaged

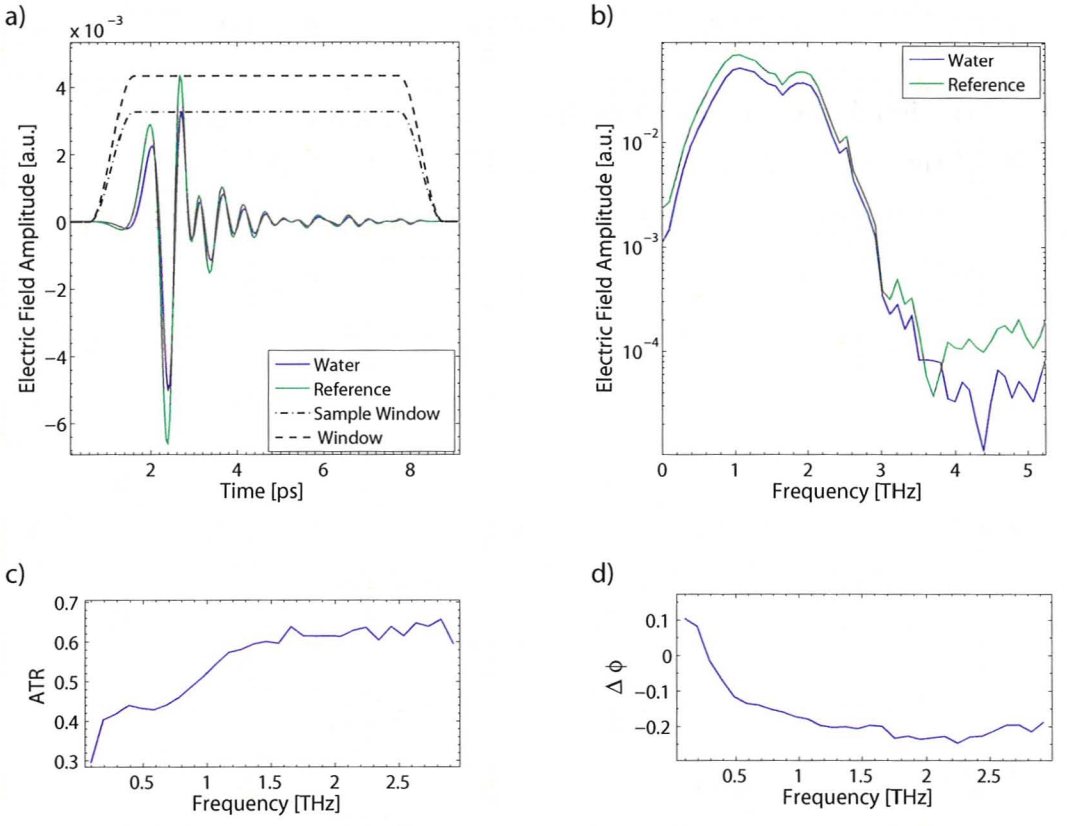

Figure 5.4: Experimental ATR data of water. **a)** Averaged temporal waveforms of the reference scans and water scans displaying their respective Tukey windows. **b)** Fourier transform of the temporal waveform displaying liquid water spectrum. **c)** ATR data and **d)** relative phase data.

regions of the detector crystal. These crucial alignment conditions need to be taken into consideration to accurately determine the generator and detector crystal angles in the future.

5.1.4 THz ATR of Sucrose Solutions

To examine the sensitivity of THz radiation to solution concentration levels, solutions of sucrose were examined. Sucrose was chosen because of the ease and convenience of preparation and sucrose solutions have been previously analyzed in the literature [51]. This was, therefore, a relatively simple experiment to ensure that our setup was sensitive to concentration change [57], and on what scale this would affect the THz

pulse. A variety of concentrations were chosen in an attempt to determine the minimal detectable concentration. As can be seen from Fig. 5.5, there is a strong attenuation in the THz signal when compared to the reference as a result of water presence on the surface of the prism. As the concentration of sugar increases, the attenuation of the THz signal decreases, implying that sucrose solutions do not absorb THz radiation as strongly as pure water.

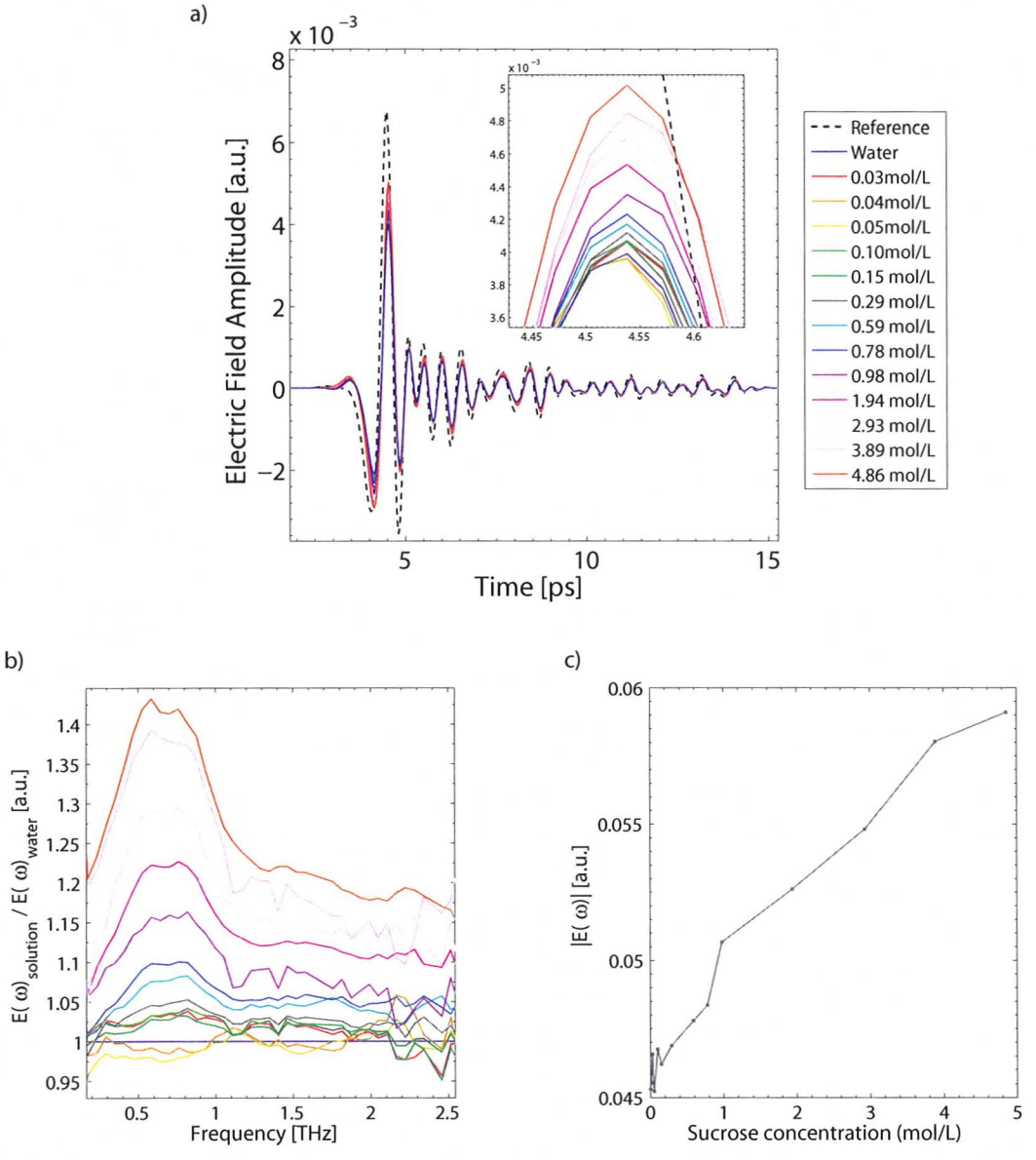

Figure 5.5: Experimental ATR data of sucrose solutions with concentrations ranging from 0.03 - 4.86 mol/L. **a)** Temporal waveform of sucrose solutions as well as the reference scan, where no sample is located on the prism, and pure water. The inset shows a close-up of the THz temporal waveform peak. **b)** Frequency spectra of the sucrose solutions normalized to the water reference. **c)** Change in the electric field amplitude as a function of solution concentration at 1 THz.

Chapter 6

Optical-Pump, THz-Probe Experiments

THz radiation is sensitive to changes in transmission, reflection and absorption properties of materials due to changes in the carrier density. Consequently, THz radiation can be used to probe the carrier dynamics following an excitation event. The experiments presented in this chapter use ultra-short laser pulses to optically excite the sample while the THz pulse monitors the effects.

6.1 Transmission Pump-Probe Experiments

As an initial calibration to correlate the timing between the optical excitation pulse and the THz pulse, transmission pump-probe experiments were performed. Samples examined in this series of experiments include Si, ZnSe bulk, and ZnSe nanowires on a fused silica substrate, as shown in Fig. 6.2. When performing pump-probe experiments on a sample in a transmission setup, the THz signal is inevitably reduced when the THz pulse is propagated through the pumped sample. The pumped region of the sample generates free carriers which contribute to the increased absorption and reflection of the THz pulse [58].

6.1.1 ZnSe Nanowires

The study of nanostructures is a rapidly expanding area of physics and engineering and it has important applications in the development of emerging technology [59, 60]. The electronic and optical behavior of semiconductor-based nanostructures changes as their size is decreased below a critical value, leading to a new regime of properties that can be harnessed for the development of innovative devices. In order to further the understanding of the properties of semiconductor nanostructures, a system of ZnSe nanowires was examined as part of a project funded by CIPI. A THz probe was used to monitor the carrier dynamics of the ZnSe nanowires following optical excitation.

The ZnSe nanowire sample was provided by Dr. Harry Ruda's group at the University of Toronto. The nanowires were epitaxially grown on a Si substrate via vapour-liquid solid mechanism in the presence of a Au catalyst [61]. While pure Si is transparent to THz radiation, when the sample is pumped by the optical excitation pulse, carriers will also be excited in the Si substrate. The carrier lifetime of Si is much longer than that of ZnSe and it would be difficult to extract the lifetime of the ZnSe if this experiment were attempted with a sample deposited on a Si substrate. In an effort to circumvent the issue of optical excitation of the substrate, the nanowires were transferred to a fused silica (SiO_2) substrate by the Ruda group via the "touch" method. This allowed for the transfer of some of the nanowires, although the new sample created has a lower density "forest" than the initially grown sample [62] and it appears that the organized orientation of the wires has been sacrificed (see Fig. 6.1).

The band gap of ZnSe is 2.70 eV, corresponding to a wavelength of 460 nm. Therefore, irradiating the sample with the 800 nm pulses produced by the laser will simply result in the transmission of the pump pulse, rather than the absorption and excitation of free carriers, unless the 800 nm excitation beam was sufficiently focused to induce two-photon transitions. A β-BBO crystal was placed in the 800 nm beam path to generate 400 nm blue light through SHG. A dielectric mirror for blue light was used in place of the first beam splitter, which splits the incoming beam into the pump beam and the THz beam (see Fig. 3.4). The dielectric mirror diverts all the blue light to the optical pump beam path while allowing the transmission of the remaining 800 nm light to be used for THz generation and detection. The sample

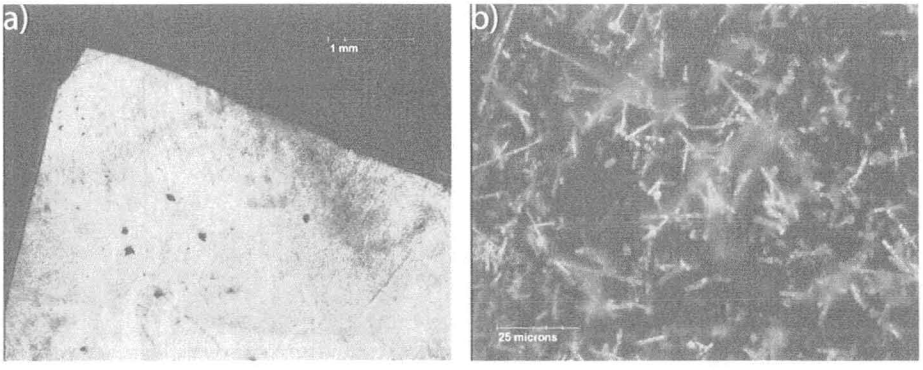

Figure 6.1: Optical microscope images of ZnSe sample on SiO_2 substrate courtesy of Eugene Hsu. **a)** Corner of the sample displaying the varying density of the nanowires on the substrate. When performing the experiment, efforts were made to examine the denser region. **b)** Close-up of one of the more dense regions of the sample. The wires appear to be much larger in diameter than quoted by the Ruda group, however this is most likely a focusing issue with the microscope.

was irradiated with ~5 mW of 400 nm light at a 500 Hz repetition rate. Because of the weak signal obtained from this sample, it is difficult to interpret from the data whether the observed offset is a real feature of the sample and the result of a longer lifetime component, or if it is electronic noise.

6.2 Reflection Pump-Probe Experiments

Unlike a transmission pump-probe experiment where the entrance facet of the sample is being pumped, and the excited carriers result in THz reflection, effectively decreasing the measured THz signal, reflection should have the opposite effect. By optically exciting the sample, the free carriers create a transient mirror which subsequently reflects more THz radiation than the unpumped sample, increasing the measured THz signal.

The optical-pump, THz-probe technique was integrated with the reflection geometry by optically exciting a silicon wafer that was placed on the reflection sample stage (see Fig. 3.5). Fig. 6.3 b) shows the reference scan acquired from the unpumped sample as well as the difference between the scans obtained at various times after the initial excitation of the sample and the reference. The difference between the pumped

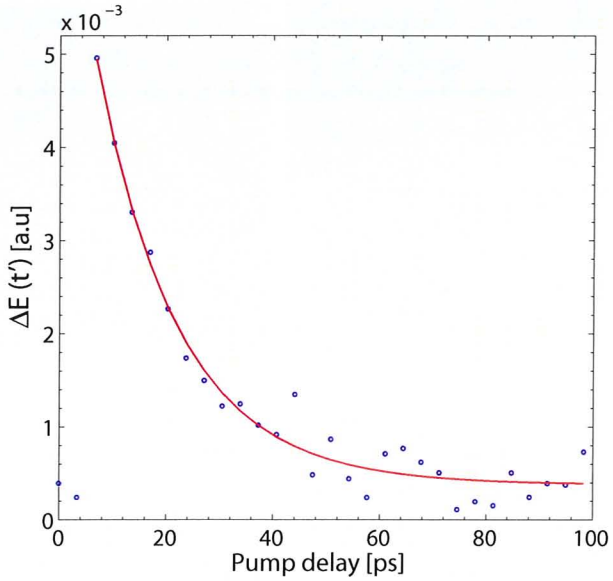

Figure 6.2: ZnSe nanowires on a fused silica substrate were pumped with ~5 mW of 400 nm at 500 Hz with a ~1 mm^2 spot size. Plotted is the change in the electric field at 1 THz. An exponential fit gives a lifetime of 15.5 ps.

sample and reference scan (ΔE) has the same sign as the temporal waveform of the reference scan, indicating that the reflected THz signal has increased as a result of pumping. The phase shift in the THz signal when the sample is being pumped is possibly the result of the optical excitation causing the Si to behave as a transient metal rather than a semiconductor. Reflection off an insulator would result in no phase shift, while reflection off a metallic surface would cause a 180° phase shift. Here we are observing an intermediate phase shift.

6.3 ATR Pump-Probe Experiments

Incorporating the optical-pump, THz-probe technique into the ATR setup is substantially more complicated than with the other geometries. Because the sample is placed directly on the surface of the prism, optically exciting the sample results in the prism being optically excited as well. Therefore, in order to properly interpret the data, a firm understanding of the carrier dynamics of the prism is required. Another complication of applying this technique is that the incident angle at which the surface of

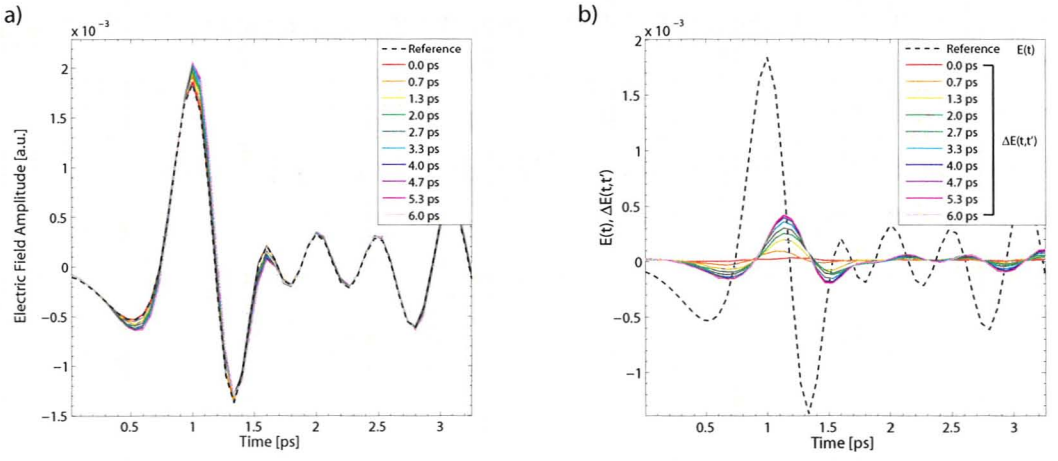

Figure 6.3: Optical-pump, THz-probe of silicon wafer in reflection geometry. **a)** Temporal waveforms from the unpumped silicon (which is the reference), and the silicon at various pump delay times. **b)** Temporal waveform of the reference scan and the difference between the pumped and the unpumped waveforms (ΔE)

the prism is pumped is not necessarily the same as the angle that the THz radiation interacts with the surface of the prism. In the transmission and reflection geometries, the pump beam is roughly collinear to the THz beam. In ATR configuration, the collinear propagation of the THz beam and the 800 nm pump beam is not possible as 800 nm light does not propagate through bulk Si. Therefore, it is necessary to ensure that the pump beam only interacts with the top surface of the prism when working with 800 nm optical pulses so as not to optically excite the front face of the prism that the THz radiation is incident upon.

To facilitate an understanding of the optical excitation response of the prism, pump-probe experiments were conducted with no sample present on the prism surface. The original intent of this experiment was to understand the behavior of the prism following optical excitation such that this information could be used as a baseline for future ATR pump-probe experiments. However, several challenges arose early in the analysis of the prism. The first major issue encountered was that the carrier lifetime of the HRFZ Si, as quoted by Tydex was 3 ms, while the time between optical pump excitation pulses was 2 ms. This results in the prism being pumped before the carriers have time to relax back to the ground state. To avoid this issue, attempts were made to change the pump repetition rate by modifying the optical chopper blade such that

every 20^{th} pulse is let through rather than every second pulse. While this would have created a sufficiently long delay between excitation events to allow for the free carriers to relax, it required locking into a 50 Hz signal. Unfortunately, it was found that anything below ~100 Hz drastically reduced the signal to noise ratio. Rather than adjusting the repetition rate of the optical pulses, the surface of the silicon prism could instead be modified to reduce the carrier lifetime. By irradiating the surface of the prism with a high energy proton beam, defects were created in the near-surface region of the prism. Creating defects in the crystal lattice shortens the mean-free path of the electrons, effectively reducing the carrier lifetime [63].

6.3.1 Si Prism Proton Irradiation

The ion implantation was preformed by Dr. Andrew Knights in the Tandetron Accelerator Laboratory at the Univeristy of Western Ontario. The 1.7 MV tandem accelerator generated a ~1 MeV proton beam, which was used to implant protons roughly 20 μm into the surface of the sample. The 1/e penetration depth of 800 nm light in Si is 10 μm, therefore an implantation twice the 1/e depth was thought to be sufficient. This energy was chosen to create as many defects as possible initially to provide the shortest attainable carrier lifetime. These defects could potentially be annealed out in a controlled manner such that the carrier lifetime could be customized. While creating defects in a 20 μm deep surface region will provide the desired effect when the prism is being pumped by near-visible optical pulses, this irradiated layer will not have a substantial effect on the absorption of the THz radiation propagating through the prism, as the propagation distance through the irradiated region is much less than the wavelength of the THz radiation.

Effect of Pump Angle

The preliminary results from the 800 nm optical pump excitation of the prism showed a longer free carrier "signal rise time" than previously observed in transmission and reflection experiments. The term "signal rise time" refers to the time delay between the initial excitation and the creation of the maximum number of free carriers. It is speculated that the increased signal rise time observed in the prism is due to the pulse front of the optical excitation pulse collapsing across the surface of the prism at

a different rate than the THz pulse front. Because of the difference in the refractive indices of the media these two beams are propagating through (i.e. n_{air}=1 and n_{Si}=3.42), by pumping the prism at a more glancing angle the time difference of the two wave fronts impinging on the interface could be decreased. To test this hypothesis in a more simple geometry, an optical-pump, THz-probe experiment was performed on a silicon wafer in transmission mode using different optical pump angles.

Fig. 6.4 a) and b) show the transmission THz data of the Si wafer with the pump beam incident at 10° to the normal, while Fig. 6.4 c) and d) show the data of the silicon sample pumped at 30° to the normal. It is evident from these figures that the signal rise time is affected by the incident angle of the pump beam. When pumping at an angle of 30° to the normal, the signal rise time is ~3.0 ps, while pumping at 10° to the normal results in a signal rise time of ~1.6 ps.

In order to minimize the effect of the THz radiation interacting with the sample at an angle, the optical pump would require a glancing angle of incidence (~80° to the normal), effectively reducing the signal rise time. The pump beam incident at such a shallow angle with respect to the prism surface presents a number of problems. Firstly, the beam has to be incident such that no 800 nm light impinges on the THz entrance face of the prism. Exciting carriers on this face of the prism would result in reflection and absorption of the incoming THz beam, rather than the free carriers interacting with the THz radiation solely at the hypotenuse of the prism. The spot size of the pump beam is highly elliptical because of the angle of incidence, causing the spot to actually be longer than the top surface of the prism. When considering the angle of the pulse wave fronts; even though an 80° angle of incidence might be optimal, it is not practical unless the beam is further manipulated using cylindrical lenses to tighten the focus at the surface of the prism. Instead, pump-probe experiments were carried out using an incident angle of 60° to the normal of the prism surface.

Carrier Lifetime of Irradiated Si Prism

In order to explore the carrier dynamics of the modified prism following proton irradiation, the surface of the prism was optically excited with 800 nm pulses of varying energy. A drastic change in the carrier lifetime was observed. Rather than a lifetime on the order of ~1 ms, it was reduced to the order of ~100 ps. This new lifetime is

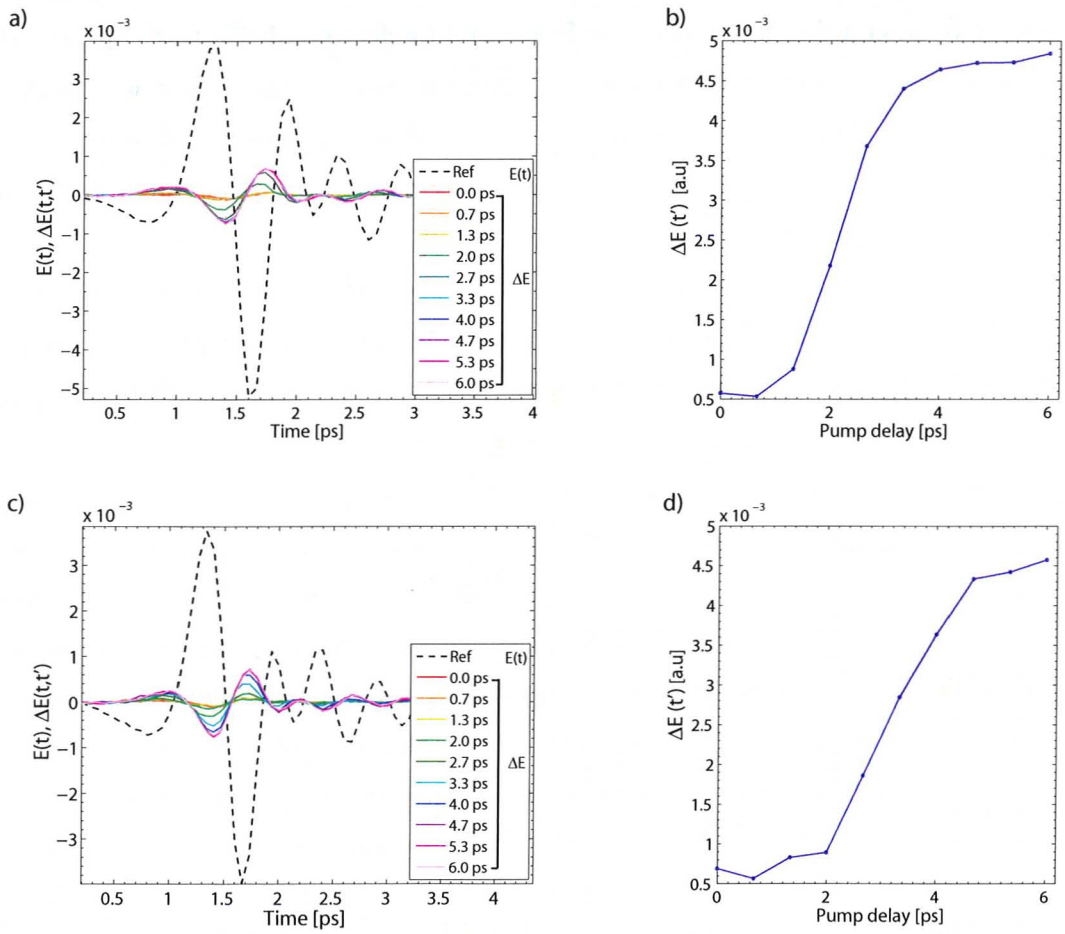

Figure 6.4: Transmission data from a Si wafer pumped with 800 nm pulses at different angles. **a)** Temporal waveform of the reference scan and the difference between the pumped and the unpumped waveforms (ΔE) at various pump delay times where the sample is pumped at 10° to the normal. **b)** Change in the electric field at 1 THz following optical excitation, displaying a signal rise time of ~1.6 ps when the wafer is pumped at 10°. **c)** Temporal waveform of the reference scan and the difference between the pumped and the unpumped waveforms (ΔE) when the sample is pumped at 30° to the normal. **d)** Change in the electric field at 1 THz following optical excitation, displaying a signal rise time of ~3.0 ps when the wafer is pumped at 30°.

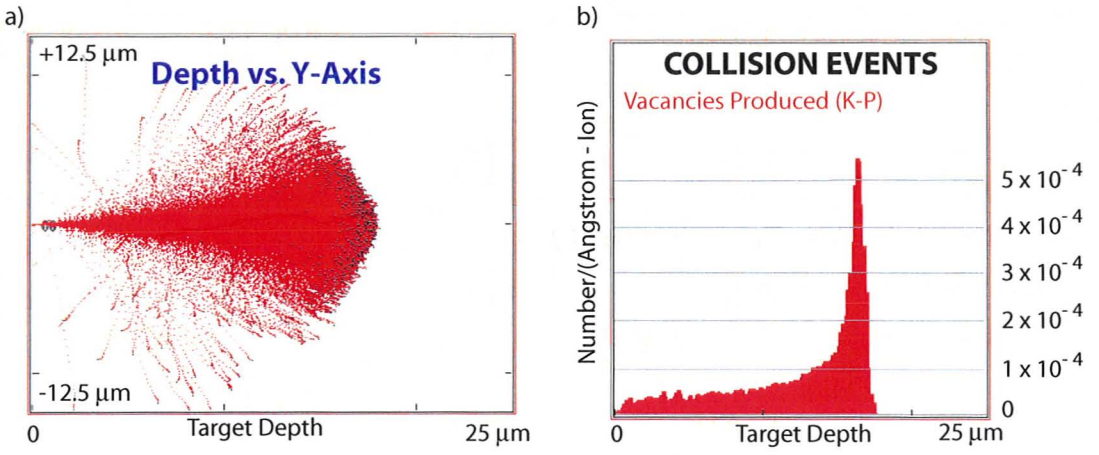

Figure 6.5: Output of SRIM showing the implantation of H^+ into Si at 1 MeV. **a)** Penetration depth of the implanted protons. **b)** Distribution of primary collision events resulting in defects.

consistent with the lifetime predicted by a theoretical calculation taking into consideration the number of defects created by the proton irradiation. The recombination rate, R, of the free carriers can be determined from

$$R = v_{th}\sigma_n n N_t(1 - F); \tag{6.1}$$

where v_{th} is the thermal velocity ($\sim 10^7$ cm/s) and σ_n is the capture cross-section ($\sim 10^{-15}$ cm^2) [63]. The number of free carriers excited, n, can be determined from the laser fluence. As 800 nm light has a 1/e penetration depth of $\sim$10 μm, a 10 μJ pulse with a 5 mm^2 spot size will excite $\sim 10^{18}$ electrons/cm^3. N_t is the number of defect centers created in the proton irradiation process. This value can be determined using the ion beam fluence in conjunction with the Monte Carlo program, SRIM (Stopping Range of Ions in Material [64]). SRIM determines the distribution of defects from collision events in a material. For the purpose of determining the theoretical carrier lifetime, the concentration of defects at the 10 μm range will be considered, as this is the 1/e penetration depth of the 800 nm light. While $\sim 4\times 10^{-5}$/Å·ion is the concentration of defects created by the proton irradiation (see Fig. 6.5), not all of these defects are stable and many of these newly created vacancies will recombine as the irradiated sample cools back down to room temperature. At room temperature

only 5-10% of the initially created defects will remain [65]. The Fermi distribution function is given by

$$F = \frac{1}{1 + e^{(E_t - E_F)/kT}}; \tag{6.2}$$

where E_t is the energy level of the defect center and E_F is the Fermi level. F can be neglected as $E_t - E_F \gg kT$, for kT at room temperature [63]. By dividing the number of free carriers excited by the optical pulse by the recombination rate, the free carrier lifetime can be determined;

$$\begin{aligned} \tau = \frac{n}{R} &= \frac{1}{v_{th}\sigma_n N_t} \\ &= \frac{1}{(10^7 cm/s)(10^{-15} cm^2)(10^{18} cm^{-3})} \\ &= 10^{-10}\ s = 100\ ps. \end{aligned} \tag{6.3}$$

Preliminary results show that there is a trend in the carrier lifetime as a function of pump power. Fig. 6.6 shows two curves, as this experiment was performed first with increasing pump pulse energy, and then with decreasing pump pulse energy. This was done to ensure there was no annealing caused by the higher fluences. The low fluence optical pump excitations yield carrier lifetimes close to that predicted by theory (see Eq. 6.3), however there is a significant increase in the carrier lifetime as the optical pump power is increased. The implanted region of the Si prism only extends $\sim$16 μm, and while this encompasses most of the 800 nm pulse, the tail of the 800 nm pulse does penetrate into the unaffected Si. This excitation of the ultra pure Si, with its lifetime of 3 ms, could explain the offset observed at high fluences, as can been seen in Fig. 6.7. Another factor contributing to the power dependent carrier lifetime is that the optical excitation pulse is creating so many carriers that they are saturating the defect recombination sites. The lower optical pump fluences yield $\sim 10^{16}$ carriers/cm^3 and the higher fluences create $\sim 10^{18}$ carriers/cm^3. The number of available recombination sites is of the order of $\sim 10^{18}/cm^3$. There is also evidence of this effect in the carrier relaxation curve of the more energetically pumped samples, as there is a short lifetime component followed by a longer one. Initially all of the defect centers are available, resulting in fast recombination, however, the carrier lifetime lengthens in the case of saturation, as more and more of the defect centers become

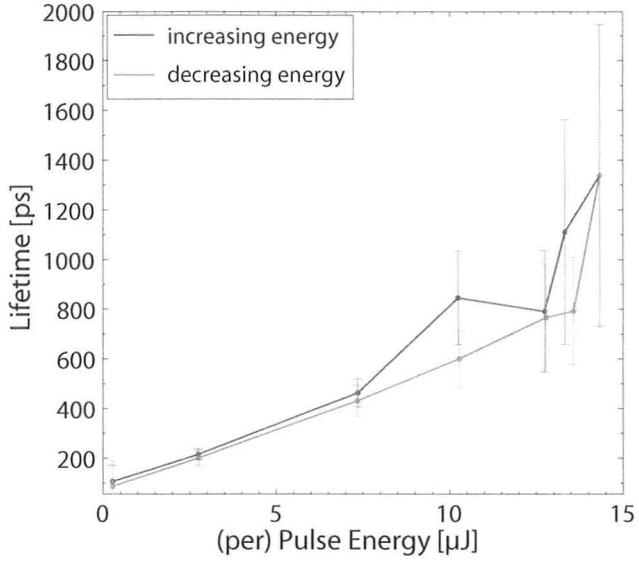

Figure 6.6: Optical-pump, THz-probe of the proton irradiated Si prism shows a decreased carrier lifetime from the undamaged Si prism; however, the lifetime does have a pump power dependence. Experiment was performed starting from low pulse energies and increasing to high pulse energies (blue curve), then decreasing back to low (green curve).

occupied. The initial fast recombination followed by a long carrier lifetime presents difficulties in determining an accurate fit to the data. The data presented in Fig. 6.7 was fit using a single exponential with an offset and the fit was started after the initial short lifetime component. As the pump energy increases the long lifetime component becomes more linear, exhibiting the effect of a recombination bottleneck. With this in mind, a more suitable model to describe the situation should be developed in future work. Unfortunately, due to the length of the long carrier lifetime component, it becomes difficult to achieve such a fit with the limited amount of data available. This problem may be rectified by incorporating a longer translation stage for the pump-probe setup to increase the length of time for data acquisition after the optical excitation pulse.

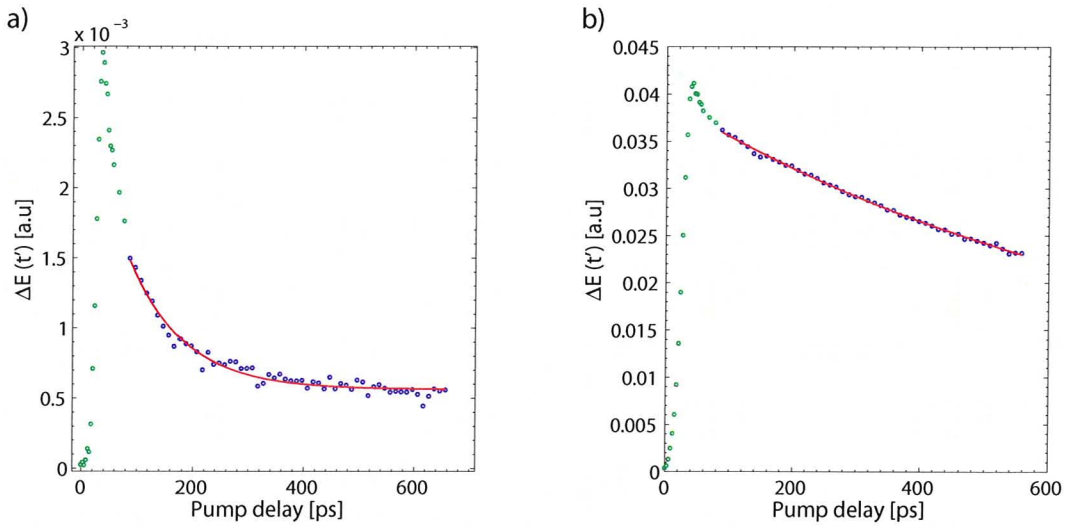

Figure 6.7: Optical-pump, THz-probe data of the irradiated Si prism. Plotted is the change in the electric field at 1 THz when the sample is pumped with 800 nm light at 500 Hz. **a)** The optical pump has a per pulse energy of 0.28 μJ and yields a carrier lifetime of 104 ps. **b)** The optical pump has a per pulse energy of 10.2 μJ and yields a carrier lifetime of 844 ps.

Chapter 7

Future Work and Concluding Remarks

7.1 Future Work

7.1.1 Temperature and Humidity Control

Incorporating temperature control capabilities to any of the experimental configurations could lead to a variety of interesting experimental opportunities, such as the examination of samples in varying degrees of hydration [66]. As THz radiation has such a strong sensitivity to water, it can be used to probe the dehydration kinetics of a system [67]. Temperature control can also lead to the observation of changes in the absorption of THz radiation as a material undergoes a phase transition. In the case of water, THz radiation is strongly absorbed due to the excitation of rotational modes of the molecules [68]. As water freezes the rotational motion of the molecules is restricted, thus the decrease in the absorption of THz radiation could be monitored [51].

7.1.2 THz ATR

Although the initial THz ATR spectroscopy experiments did not yield results that were in agreement with the literature, valuable insight has been gained as to how to approach the problems that have been encountered.

The polarization of the THz pulse is certainly a contributing factor to the difficulties encountered in interpreting the data. The form of analysis used to extract the dielectric constant, and other subsequent optical constants, relies on the fact that the THz radiation incident on the top surface of the prism is p-polarized. The next obvious step for this project is to ensure that the polarization of the THz radiation is well characterized and, preferably, is made as linear as possible. This can be done by rigorously mapping out the generator and detector crystals. In this particular THz setup, it would be advantageous to replace the detector crystal, as the current detector crystal does have some damaged areas. The linear polarization of the THz beam can be further purified by incorporating a wire grid polarizer immediately after the ZnTe generator crystal.

Another important factor that needs to be resolved in order to progress with ATR spectroscopy is the optimization of the absorption of THz radiation by a sample placed on the prism. The data presented in Chapter 5 shows that when water is placed on the surface of the prism the signal is attenuated, resulting in a ATR signal that ranges from 0.3 - 0.7 (see Fig. 5.4), while the ATR signal for water presented by Nagai ranged from 0 - 0.5 [51]. As these results were obtained under very similar conditions, this discrepancy in the absorption is unexpected. While the polarization does affect the overall absorption, another potential cause of the lack of attenuation in the THz signal is the alignment and focusing of the THz beam on the sample. It is possible that, because of the larger focal diameter of the low frequency THz components, part of the THz spot is incident on the region of the prism surface outside of the fluid cell. This would effectively lower the observed index of refraction of the water as the measurement would actually be a combination of water, air and glass from the fluid cell wall.

The angle of the THz beam as it impinges on the prism surface is another area of concern. The prism was designed such that light propagating parallel to the optics table would enter the prism and interact with the top surface at an angle greater than the critical angle for samples below a refractive index of 2.67. Not only is it difficult to be certain that the incoming beam is propagating parallel to the table, but the prism was design under the assumption that the THz beam was collimated. Since the THz beam is being focused, there is a small range of angles at which the

beam is interacting with the surface. This could potentially lead to some of the THz radiation being incident at an angle greater than assumed from the critical angle, leading to a reduced effective thickness of the evanescent wave, or possibly less than the critical angle, causing partial transmission. Both of these scenarios would reduce the absorption of the THz radiation by the sample and could contribute to the difference in the observed results from the literature.

The solution to these problems lie in rigorous, tedious alignment to ensure that the focus of the THz spot is not only as tight as possible, but also located at the prism surface. It may be advantageous to re-evaluate the prism geometry to ensure the TIR conditions are met by accommodating the level of uncertainty in the incident THz beam angle. Longer focal length off-axis parabolic mirrors would help reduce the range of angles of the incident THz beam, however this could increase the effects of spherical aberration, reducing the intensity of the THz beam at the focus. If these efforts could be employed to maximize the absorption of the THz radiation on the prism surface it could lead to the successful characterization of the optical properties of water, which would open up many possibilities for future studies of biological systems in their naturally hydrated state [69, 70, 71].

7.1.3 ZnSe Nanowires

Should the ZnSe nanowire samples be pursued and re-examined, there are a few changes that, if implemented, could increase the quality of the sample and the quality of the data obtained from the sample. A source of the weak signal observed was that the prepared samples did not have sufficient quantum wire material on them. As there was no direct involvement with the sample preparation, this is mostly speculation as to how the density of nanowires could be increased. One possibility is to grow the nanowires on a Si substrate, as per normal, but then sonicate the sample in an attempt to create a concentrated suspension of nanowires. This suspension could then be evaporated down onto a SiO_2 substrate. Another possibility would be to use a polymer tape to remove the nanowires from the Si substrate. This would likely remove more nanowires than merely touching a fused silica slide to the sample and the polymer tape should not present a problem when irradiated with the optical pump beam. These sample improvement tactics were not applied due to time constraints.

From the point of view of the laser-based experiment, the sample could be pumped with a higher power of 400 nm to excite more carriers.

7.1.4 ATR Pump-Probe

All of the work presented in this thesis with regards to optical-pump, THz-probe in the ATR geometry used 800 nm light to excite the prism so its response could be characterized. The issue of optically exciting the prism as well as the sample could be circumvented by using a longer wavelength optical pump. The Spectra-Physics Ultrafast kHz Optical Parametric Amplifier available in the lab can generate wavelengths from ~1.15 μm - 2.62 μm [72]. As these wavelengths are below the band gap of Si (1.11 eV, 1.1118 μm), they can freely propagate through the prism. This allows for the possibility of collinear propagation of the optical pump and the THz beam through the prism. In this configuration, the sample would be optically excited by the evanescent wave generated by the pump beam, causing only excitation to the material in the near surface region of the prism.

Another way to examine the carrier dynamics in the near surface region of the Si is to employ the same pump-probe configuration as the work presented in Section 6.3, pumping the top surface of the prism, with a 400 nm optical excitation pulse. The penetration depth of 400 nm light is much less than 800 nm [73], thus free carriers would only be excited near the surface.

7.1.5 Ion Implanted Prism

The pump-probe experiment discussed in this thesis is the first step of a series of experiments that could potentially be pursued. The defects created through the proton implantation process can be gradually removed by annealing the prism in stages. This allows for the possibility of customizing the carrier lifetime in the near surface region of the prism. In an effort to determine a more accurate fit for the long lifetime component of the free carrier lifetime, the optical pump translation stage should be extended. Because of the long lifetime of Si, it would be beneficial to have more than 666 ps of delay after the optical excitation pulse.

While it was not the original intent of the project, the characterization of the

carrier dynamics of high purity HRFZ Si is an area of interest. This experiment could then be reproduced examining the effects of different energies of proton implantation. Another possible experimental avenue would be to irradiate the prism surface with Si ions. This would create much more damage in the very near surface region, $< 5\mu$m. Appendix C details these possible scenarios, which should be considered if future work in this area is pursued. There are, of course, other ion implantation possibilities other that H^+ and Si^+, however these two are the least intrusive.

7.2 Conclusions

The experimental work presented in this thesis relates to the construction and development of a versatile, multi-functioning THz system and the preliminary data obtain from this setup. The different experimental geometries can function to obtain spectroscopic information, through THz time-domain spectroscopy, or to study the carrier dynamics of system following optical excitation.

A large portion of this project was dedicated to the development of a THz system which could operate in several modes to accommodate different experimental situations. It is capable of functioning in a standard transmission mode, which is useful for samples that are not strongly absorbing and have a uniform thickness. Having a transmission THz system also simplifies the overall alignment process initially performed before any experimentation. The system can easily be converted into reflection mode with the use of an aluminum reflector piece, which was machined to divert the THz beam line to reflect off of the surface of a sample. While this reflector piece is just a crude prototype, preliminary data using this component was presented in Chapters 4 and 6, demonstrating its functionality. The system can also operate in an ATR mode by totally internally reflecting the THz beam through a HRFZ silicon prism. In this configuration, samples that are placed on the surface of the prism will be probed by the THz evanescent wave, attenuating the THz signal.

The efforts involving the ATR configuration proved to be much more challenging. While ATR THz signals were obtained with the prism, obtaining the expected literature values proved elusive. Water was the primary test sample for the preliminary THz ATR experiments. The presence of water on the surface of the prism did re-

sult in substantial attenuation of the THz signal, however this attenuation was not as strong as anticipated, resulting in a higher ATR value and lower refractive index than expected.

The optical-pump, THz-probe capabilities were successfully coupled to the transmission and reflection geometries. Although the pump-probe experiments conducted in the reflection configuration were performed primarily for diagnostic purposes, the transmission pump-probe setup was used to examine the free carrier lifetime of ZnSe nanowires.

Attempts to couple the optical-pump, THz-probe technique with the ATR configuration were met with additional challenges. The preliminary experiments were intended to characterize the carrier lifetime following optical excitation of the Si prism. Knowledge of the carrier dynamics of the prism is crucial if optical-pump THz ATR-probe experiments are to be conducted later. The HRFZ Si has a carrier lifetime which is longer than the time between optical excitations. In an effort to control the carrier lifetime in the near surface region, the hypotenuse of the prism underwent proton irradiation to increase the number of defects and effectively shorten the lifetime. The proton irradiation was successful in decreasing the carrier lifetime, however a pump power dependent carrier lifetime was observed. From an order magnitude calculation of the number of defects created in the Si, this is most likely due to the saturation of recombination sites. When the prism is pumped with a high enough power such that the number of free carriers approaches the number of available recombination sites, the carrier lifetime is inevitably increased.

Appendix A

Circuit Diagrams

A.1 Photodiode Biasing Network

As a standard electronics practice, current limiting resistors are employed in this circuit (330 Ω resistors). 470 μF electrolytic and 47 nF ceramic capacitors are used to smooth out minor ripples. The photodiodes are reverse-biased such that they are in photoconductive mode, allowing fast operation and providing a linear output as a function of illuminance.

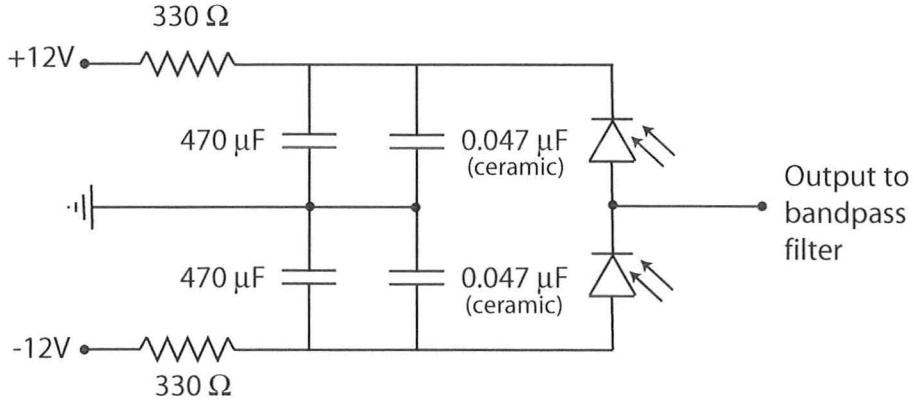

Figure A.1: Photodiode detector circuit.

A.2 Op-amp Based Active Bandpass Filter

A bandpass filter is used to prevent higher harmonics of the signal from overloading the lock-in amplifier. An active filter is chosen over a passive filter network since its high input impedance and low output impedance can act as a buffer between the photodiode biasing network and any output stage following the filter. By using an active filter, passive components such as the inductor, which is prone to and can actually create, electromagnetic interference, can be avoided. An RC network (referring to the 15 kΩ, 750 Ω, 295 kΩ resistors and the 22 nF capacitors) was built around the op-amp to determine the corner frequency of the bandpass filter. A voltage divider (referring to the 4.7 kΩ and 540 Ω resistors) at the output stage sets the overall gain to unity.

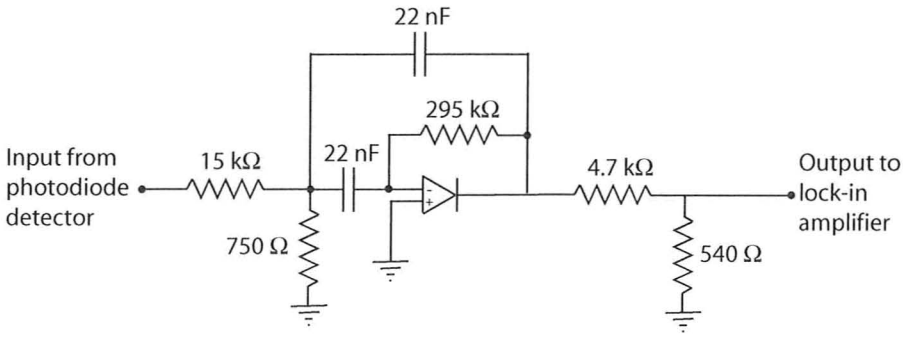

Figure A.2: Bandpass filter circuit.

Appendix B

THz ATR

B.1 Optical Properties of Water

In Section 5.1.3 the THz ATR data for water was presented, as well as a method of analysis for determining certain optical properties from the data. Using this data and analysis, the complex dielectric function was calculated, and from this the refractive index and extinction coefficient could be extracted. While the results for the optical properties of water, presented in Fig. B.1, are not in agreement with the literature [51], Section 5.1.3 provides a detailed discussion as to what could be causing these discrepancies.

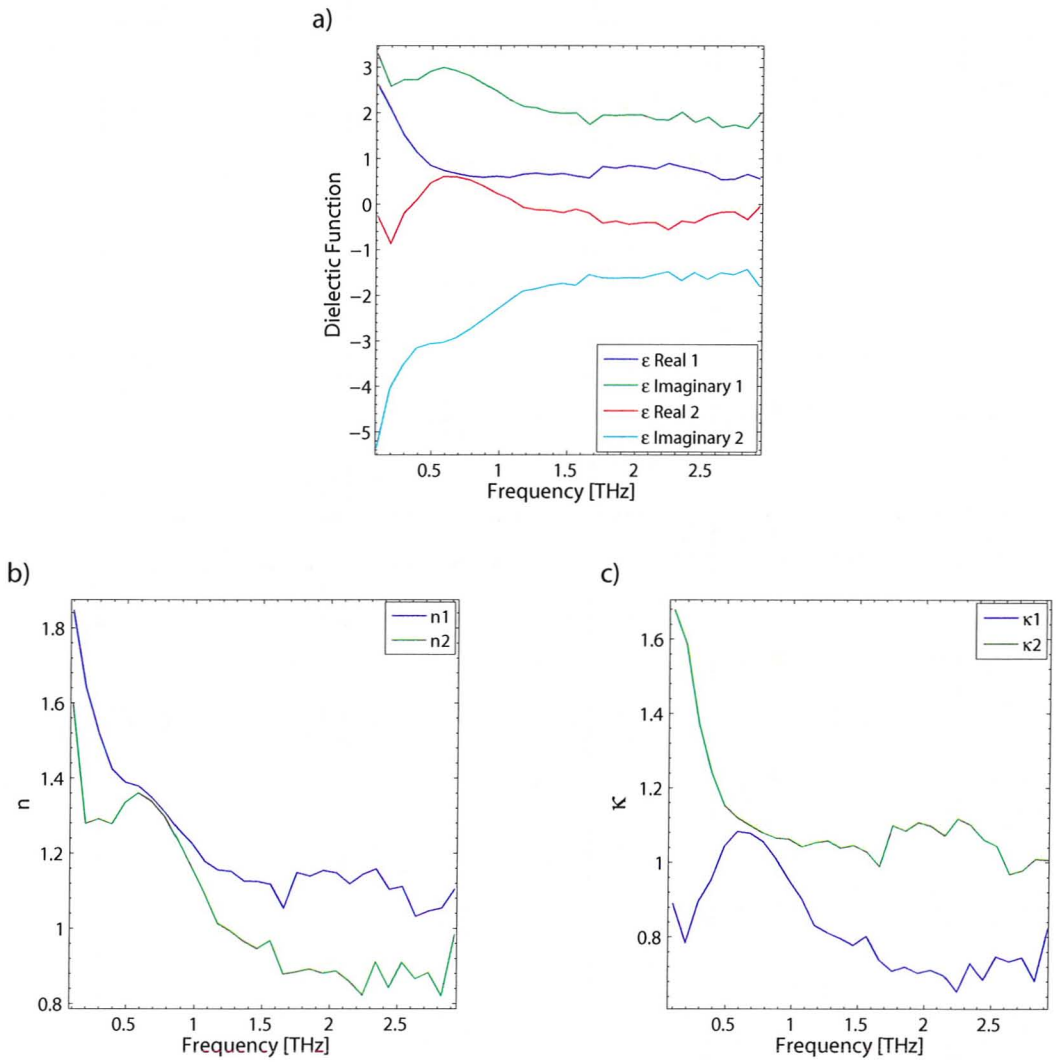

Figure B.1: **a)** Calculated dielectric function of water, displaying both the positive and negative roots. **b)** Refractive index of water, calculated from the positive and negative roots of the dielectric function. **c)** Extinction coefficient of water, calculated from the positive and negative roots of the dielectric function.

Appendix C

Ion Implantation Future Work

The proton implantation presented early in this thesis was performed at 1 MeV and created defects in the near surface region of the prism that ranged up to a ~16 μm depth. (It should be noted that SRIM calculated the ion trajectories assuming the irradiated material is amorphous Si. Because the Si used in these experiments is crystalline, it is possible that the ions could be channeled through the crystal lattice resulting in a deeper than calculated penetration depth.) While the 1/e penetration depth of 800 nm light into Si is ~10 μm, at the higher pump powers there is still some significant penetration of 800 nm light into the undamaged Si (see Fig.C.1). If further experimentation regarding ion implantation is pursued, Fig. C.2, Fig. C.3, and Fig. C.4 display three possible scenarios that may be explored.

It would be interesting to attempt irradiating the prism with higher energy protons resulting in a larger implant depth (see Fig. C.2). This may help elucidate how much of the observed offset in the carrier lifetime was due to saturation of recombination sites and how much was a result of excitation of the undamaged long carrier lifetime Si.

Another possible approach would be to use a low proton beam energy to increase the number of defects in the region where there is the highest intensity of 800 nm light (see Fig. C.3). This concept could be taken one step further by irradiating the surface of the prism with Si ions (see Fig C.4). These systems maybe interesting to study using a 400 nm optical excitation pulse due to the large number of defects created in the near surface region of the Si, particularly in the case of Si^+ irradiation.

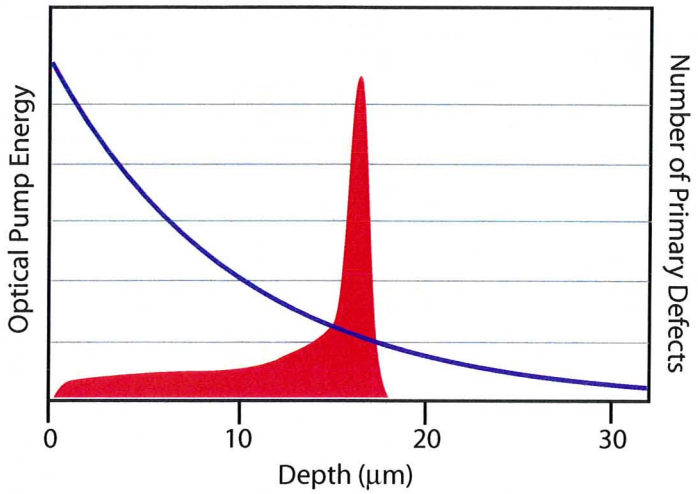

Figure C.1: Penetration depth of the 800 nm optical excitation pulse (blue) into the Si sample with respect to the defect distribution caused by the 1 MeV proton beam (red).

The 400 nm light has a 1/e penetration depth on the order of ~100 nm [73], which would be well within the region of damaged Si.

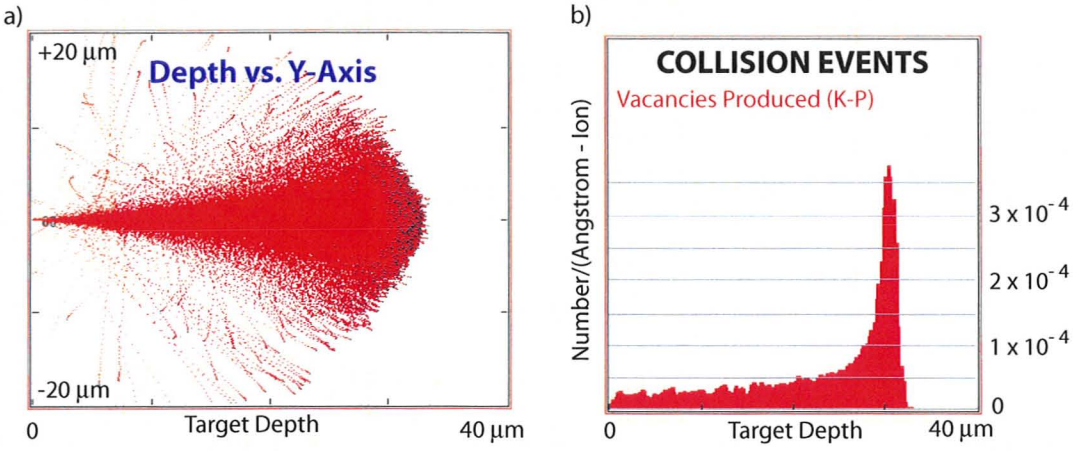

Figure C.2: Output of SRIM showing the implantation of H^+ into Si at 1.5 MeV. **a)** Penetration depth of the implanted protons. **b)** Distribution of primary collision events resulting in defects.

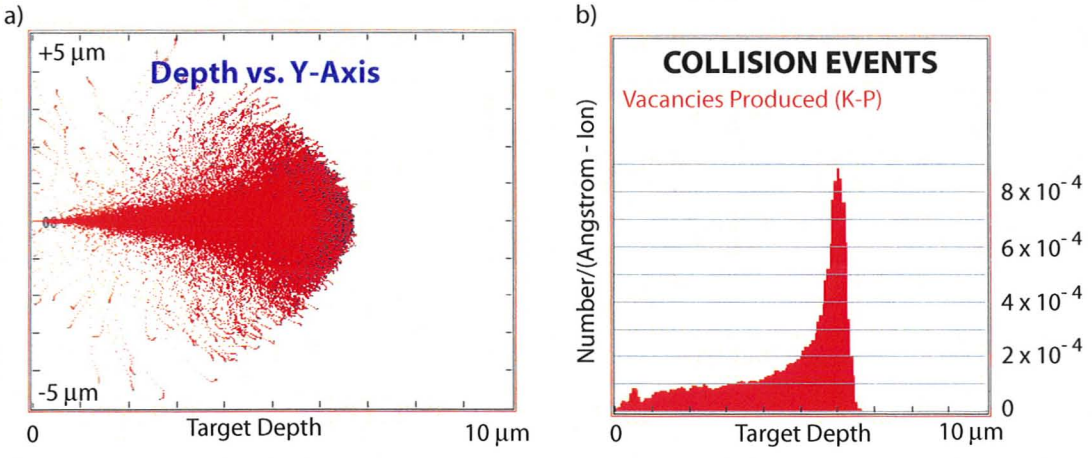

Figure C.3: Output of SRIM showing the implantation of H^+ into Si at 500 keV. **a)** Penetration depth of the implanted protons. **b)** Distribution of primary collision events resulting in defects.

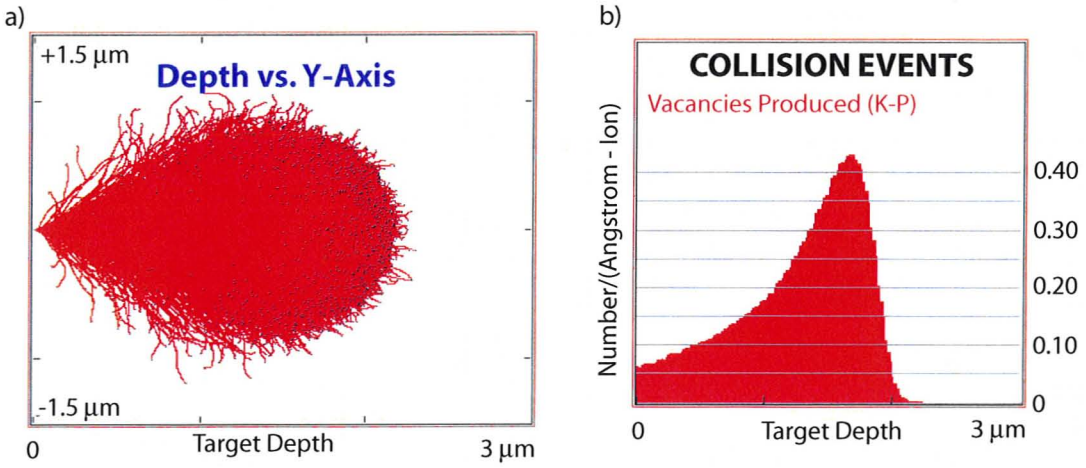

Figure C.4: Output of SRIM showing the implantation of Si ions into Si at 2 MeV. **a)** Penetration depth of the implanted Si ions. **b)** Distribution of primary collision events resulting in defects.

Bibliography

[1] B. Ferguson and X.-C. Zhang. Materials for Terahertz Science and Technology. *Nature Materials*, 1:26, September 2004.

[2] A. Dobroiu, C. Otani, and K. Kawase. Terahertz-wave sources and imaging applications. *Measurement Science and Technology*, 17:161, September 2006.

[3] E. Pickwell and V.P.Wallace. Biomedical applications of terahertz technology. *Journal of Physics D: Applied Physics*, 39:301, August 2006.

[4] M. Hangyo, M. Tani, and T. Nagashima. Terahertz Time-Domain Spectroscopy of Solides: A Review. *International Journal of Infrared and Millimeter Waves*, 26:1661, December 2005.

[5] C.A. Schmuttenmaer. Exploring Dynamics in the Far-Infrared with Terahertz Spectroscopy. *Chemical Review*, 104:1759, September 2004.

[6] M.C. Beard, G.M. Turner, and C.A. Schuttenmaer. Terahertz Spectroscopy. *Journal of Physical Chemistry B*, 106:7146, May 2002.

[7] T. Mori, E.J. Nicol, S. Shiizuka, K. Kuniyasu, T. Nojima, N. Toyota, and J.P. Carbotte. Optical optical self-energy of superconducting Pb in the terahertz region. *Physical Review B*, 77:174515, May 2008.

[8] T. Mori, S. Goshima, K. Iwamoto, S. Kushibiki, H. Matsumoto, N. Toyota, K. Suekuni, M.A. Avila, T. Takabatake, T. Hasegawa, N. Ogita, and M. Udagawa. Optical conductivity of rattling phonons in type-I clathrate $Ba_8Ga_{16}Ge_{30}$. *Physical Review B*, 79:212301, June 2009.

[9] F. Kadlec, H. Němec, and P. Kužel. Optical two-photon absorption in GaAs measured by optical-pump terahertz-probe spectroscopy. *Physical Review B*, 70:125205, September 2004.

[10] R.D. Averitt, G. Rodriguez, J.L.W. Siders, S.A. Trugman, and A.J. Taylor. Conductivity artifacts in optical-pump THz-probe measurements of $YBa_2Cu_3O_7$. *Journal of the Optical Society of America B*, 17:327, February 2000.

[11] A.K. Kristoffersen, H. Tiedje, R.A. Hughes, H.K. Haugen, and J.S. Preston. Terahertz pump-probe spectroscopy in YBCO thin films. *Proceeding of SPIE*, 5579:750, November 2004.

[12] D.H. Wu and J.R. Meyer. Terahertz Emission, Detection and Military Applications. *Proceedings of SPIE*, 5411:187, April 2004.

[13] P.R. Smith, D.H. Auston, and M.C. Nuss. Subpicosecond Photoconducting Dipole Antennas. *IEEE Journal of Quantum Electroncs*, 24:255, February 1988.

[14] C. Fattinger and D. Grischkowsky. Terahertz beams. *Applied Physics Letters*, 54:490, February 1989.

[15] Y.C. Shen, P.C. Upadhya, E.H. Linfield, H.E. Beere, and A.G. Davies. Ultrabroadband terahertz radiation from low-temperature-grown GaAs photoconductive emitters. *Applied Physics Letters*, 83:3117, October 2003.

[16] Y.C. Shen, P.C. Upadhya, H.E. Beere, E.H. Linfield, A.G. Davies, I.S. Gregory, C. Baker, W.R. Tribe, and M.J. Evans. Generation and detection of ultrabroadband terahertz radiation using photoconductive emitters and receivers. *Applied Physics Letters*, 85:164, July 2004.

[17] R.W. Boyd. *Nonlinear Optics, 2^{nd} Edition.* Academic Press, 1996.

[18] E. Hecht. *Optics, 4^{th} Edition.* Pearson Education, Inc., 2002.

[19] M.D. Thomson, Markus Kreβ, T. Löffler, and H.G. Roskos. Broadband THz emission from gas plasmas induced by femtosecond optical pulses: From fundamentals to applications. *Laser and Photon Review*, 1:349, November 2007.

[20] P.H. Bucksbaum, R.R. Freeman, M. Bashkansky, and T.J. McIlrath. Role of ponderomotive potential in above-threshold ionization. *Journal of the Optical Society of America B*, 4:760, May 1987.

[21] H. Hamster, A. Sullivan, S. Gordon, W. White, and R.W. Falcone. Subpicosecond, Electromagnetic Pulses from Intense Laser-Plasma Interaction. *Physical Review Letters*, 71:2725, October 1993.

[22] H. Hamster, A. Sullivan, S. Gordon, and R.W. Falcone. Short-pulse terahertz radiation from high-intensity-laser-produced plasmas. *Physical Review E*, 49:671, January 1994.

[23] T. Löffler, F. Jacob, and H.G. Roskos. Generation of terahertz pulses by photoionization of electrically biased air. *Applied Physics Letters*, 77:453, July 2000.

[24] D.J. Cook and R.M. Hochstrasser. Intense terahertz pulses by four-wave rectification in air. *Optics Letters*, 25:1210, August 2000.

[25] M. Kress, T. Löffler, S. Eden, M. Thomson, and H.G. Roskos. Terahertz-pulse generation by photoionization of air with laser pulses composed of both fundamental and second-harmonic waves. *Optics Letters*, 29:1120, May 2004.

[26] X. Xie, J. Dai, and X.-C. Zhang. Coherent Control of THz Wave Generation in Ambient Air. *Physical Review Letters*, 96:075005, February 2006.

[27] K. Reimann. Table-top sources of ultrashort THz pulses. *Reports on Progress in Physics*, 70:1597, September 2007.

[28] J. Dai, X. Xie, and X.-C. Zhang. Detection of Broadband Terahertz Waves with a Laser-Induced Plasma in Gases. *Physical Review Letters*, 97:103903, September 2006.

[29] K.Y. Kim, J.H. Glowina, A.J. Taylor, and G. Rodriguez. Terahertz emissions from ultrafast ionizing in symmetry-broken laser fields. *Optics Express*, 15:4577, April 2007.

[30] Q. Wu and X.-C. Zhang. Free-space electro-optic sampling of terahertz beams. *Applied Physics Letters*, 67:3523, December 1997.

[31] C. Winnewisser, P. Uhd Jepsen, M. Schall, V. Schyja, and H. Helm. Electro-optic detection of THz radiation in $LiTaO_3$, $LiNbO_3$, and ZnTe. *Applied Physics Letters*, 70:3069, June 1997.

[32] P.C. Planken, H-K Nienhuys, H.J. Bakker, and T. Wenckebach. Measurement and calculation of the orientation dependence of terahertz pulse detection in ZnTe. *Journal of the Optical Society of America B*, 18:313, March 2001.

[33] J. Hebling, A.G. Stepanov, G. Almási, B. Bartal, and J. Kuhl. Tunable THz pulse generation by optical rectification of ultrashort laser pulses with tilted pulse fronts. *Applied Physics B*, 78:593, March 2004.

[34] F.de Fornel. *Evanescent Waves From Newtonian Optics to Atomic Optics.* Springer, 2001.

[35] M. Born and E. Wolf. *Principles of Optics, 3^{rd} Edition.* Pergamon Press, 1965.

[36] S.J F.L. Pedrotti and L.S Pedrotti. *Introduction to Optics, 2^{nd} Edition.* Prentice Hall, Inc., 1993.

[37] N.J. Harrick. *Internal Reflection Spectroscopy.* John Wiley and Sons, 1967.

[38] F.J. Harris. On the Use of Windows for Harmonic Analysis with the Discrete Fourier Transform. *Proceedings of the IEEE*, 66:51, January 1978.

[39] II L.W. Couch. *Digital and Analog Communication Systems, 6^{th} Edition.* Prentice Hall, Inc., 2001.

[40] M. van Exter, Ch. Fattinger, and D. Grischkowsky. Terahertz time-domain spectroscopy of water vapor. *Optics Letters*, 14:1128, October 1989.

[41] Spectra-Physics Lasers. *Millennia Vs: Diode-pumped, cw Visible Laser, User's Manual.*

[42] Spectra-Physics Lasers. *Tsunami: Mode-locked Ti:sapphire Laser, User's Manual.*

[43] Spectra-Physics Lasers. *Spitfire: Kilohertz, 50fs, Ti:sapphire Laser Amplifier, User's Manual.*

[44] Spectra-Physics Lasers. *Evolution: Intracavity Doubled, Diode-Pumped Nd:YLF Laser, User's Manual.*

[45] G. Mourou. The ultrahigh-peak-power laser: present and future. *Applied Physics B*, 65:205, June 1997.

[46] Spectra-Physics Lasers. *Spitfire: Multikilohertz Pulsed Ti:sapphire Amplifier with Pulse Stretcher and Compressor, User's Manual.*

[47] A. Yariv. *Quantum Electronics, 2nd Edition.* John Wiley and Sons, 1975.

[48] Q. Wu, M Litz, and X.-C. Zhang. Broadband detection capability of ZnTe electro-optic field detectors. *Applied Physics Letters*, 68:2924, May 1996.

[49] G. Zhao, R.N. Schouten, N. van der Valk W. Th. Wenckebach, and P.C.M. Planken. Design and preformance of a THz emission and detection setup based on a semi-insulating GaAs emitter. *Review of Scientific Instruments*, 73:1715, April 2002.

[50] H. Hirori, K. Yamashita, M. Nagai, and K. Tanaka. Attenuated Total Reflection Spectroscopy in Time Domain Using Terahertz Coherent Pulses. *Japanese Journal of Applied Physics*, 43:1287, September 2004.

[51] M. Nagai, H. Yada, and K. Tanaka T. Arikawa. Terahertz time-domain attenuated total reflection spectroscopy in water and biological solution. *International Journal of Infrared and Millimeter Waves*, 27:505, April 2006.

[52] Tydex co. Website. `http://www.tydex.ru/en`.

[53] Y. Chen, M. Yamaguchi, M. Wang, and X.-C. Zhang. Terahertz pulse generation from noble gases. *Applied Physics Letters*, 91:251116, December 2007.

[54] D.A. Newnham and P.F. Taday. Pulsed Terahertz Attenuated Total Reflection Spectroscopy. *Applied Spectroscopy*, 62:394, January 2008.

[55] L. Thrane, R.H. Jacobsen, P. Uhd Jepsen, and S.R. Keiding. THz reflection spectroscopy of liquid water. *Chemical Physics Letters*, 240:330, June 1995.

[56] Q. Chen, M. Tani, Z. Jiang, and X.-C. Zhang. Electro-optic transceivers for terahertz-wave applications. *Journal of the Optical Society of America B*, 18:823, June 2001.

[57] T. Arikawa, K. Yamashita, H. Hirori, M Nagai, and K. Tanaka. Dynamics of Biomolecules in Water by Terahertz Time-domain Total Reflection Spectroscopy. *The Joint 30th International Conference on Infrared and Millimeter Waves and 13th International Conference on Terahertz Electronics*, 1:52, September 2005.

[58] H. F. Tiedje, H.K. Haugen, and J.S. Preston. Measurement of nonlinear absorption coefficients in GaAs, InP and Si by an optical pump THz probe technique. *Optics Communications*, 274:187, January 2007.

[59] Y. Xia, P. Yang, Y. Sun, Y. Wu, B. Mayers, B. Gates, Y. Yin, F. Kim, and H. Yan. One-Dimensional Nanostructures: Synthesis Characterization, and Applications. *Advances Materials*, 15:4577, March 2003.

[60] H.E. Ruda, J.C. Polanyi, S.Y. Yang, Z. Wu, U. Philipose, T. Xu, S. Yang, K.L. Kavanagh, J.Q. Liu, L. Yang, Y. Wang, K. Robbie, J. Yang, D.G. Cooke, F.A. Hegmann, A.J. Budz, and H.K. Haugen. Developing 1D nanostructure arrays for future nanophotonics. *Applied Physics Letters*, 1:99, August 2006.

[61] R.S. Wagner and W.C. Ellis. Vapor-Liquid-Solid Mechanism of Single Crystal Growth. *Applied Physics Letters*, 4:89, March 1964.

[62] U. Philipose, H.E. Ruda, A. Shik, C.F. de Souza, and P. Sun. Conductivity and photoconductivity in undoped ZnSe nanowire array. *Journal of Applied Physics*, 99:066106, March 2006.

[63] S.M Sze. *Semiconductor Devices - Physics and Technology.* John Wiley and Sons, 1985.

[64] James F. Ziegler. Particle Interactions with Matter. Website, 2001. `http://www.srim.org`.

[65] P.G. Coleman, C.P Burrows, and A.P. Knights. Simple expression for vacancy concentrations at half ion range following MeV ion implantation of silicon. *Applied Physics Letters*, 80:946, February 2002.

[66] J. Balakrishnan, B.M. Fischer, and D. Abbott. Sensing the hygroscpicity of polymer and copolymer materials using terahertz time-domain spectroscopy. *Applied Optics*, 48:2262, April 2009.

[67] H.-B. Liu and X.-C. Zhang. Dehydration kinetics of D-glucose monohydrate studied using THz time-domain spectroscopy. *Chemical Physics Letters*, 429:229, August 2006.

[68] H.M. Randall, D.M. Dennison, N. Ginsburg, and L.R. Weber. The Far Infrared Spectrum of Water Vapor. *Physical Review*, 52:160, May 1937.

[69] T. Arikawa, M. Nagai, and K. Tanaka. Hydration number of biomolecules evaluated with THz time-domain attenuated total reflection spectroscopy. *Conference on Lasers and Electro-Optics and Quantum Electronics and Laser Science Conference*, page 1, May 2006.

[70] B. Born, S.J. Kim, S. Ebbinghaus, M. Gruebele, and M. Havenith. The terahertz dance of water with the proteins: the effect of protein flexibility on the dynamical hydration shell of ubiquitin. *Faraday Discussions*, 141:161, October 2008.

[71] Erik Brün dermann, B. born, S. Funkner, M. Krüger, and M. Havenith. Terahertz spectroscopic techniques for the study of proteins in aqueous solution. *Proceedings of SPIE*, 7215:72150, February 2009.

[72] Spectra-Physics Lasers. *OPA: Ultrafast kHz Optical Parametric Amplifier, User's Manual.*

[73] K.P.H. Lui and F.A. Hegmann. Ultrafast carrier relaxation in radiation-damaged silicon on sapphire studied by optical-pump-terahertz-probe experiments. *Applied Physics Letters*, 78:3478, May 2001.